Numerical investigation of the hydrodynamics of a submersible steel-frame offshore fish farm in regular waves using CFD

Gang Wang[1], Tobias Martin[2], Liuyi Huang [*1], and Hans Bihs[2]

[1]College of Fisheries, Ocean University of China, 266003 Qingdao, China
[2]Department of Civil and Environmental Engineering, Norwegian University of Science and Technology (NTNU), 7491 Trondheim, Norway

Ocean Engineering, 2022, **256**, pp. 111528.
DOI: https://dx.doi.org/10.1016/j.oceaneng.2022.111528

Abstract

The hydrodynamics and non-linear interaction between the submersible steel-frame offshore fish farm "ShenLan 1" and regular waves are investigated using the open-source CFD toolbox REEF3D. The effects of the regular wave parameters, different net sheets, and structural variations on the motion responses and mooring forces of the fish farm system are studied. The numerical framework consists of a moored-floating body motion solver for the frame structure coupled to a fluid dynamics solver to simulate the two-phase propagation of the waves. The momentum loss of the flow over fixed net sheets is included in the solver. First, the chosen model is validated for a coupled rigid body motion and net hydrodynamics. Then, the solver is applied to the offshore fish farm "ShenLan 1". It is shown that the surge motions are more sensitive to the wave parameters compared to the heave and pitch motions due to the restrain from the mooring system. In contrast to the vertical components, the horizontal loadings positively correlate with the wave heights and periods. The nets show minor influence on the motion responses, but the percentage of horizontal forces attributed to nets decreases from 55% to 10% in larger wave periods. The translational motions, as well as mooring restoring tensions, are particularly sensitive to shifts of the draught. Finally, the increase of the aspect ratio of "ShenLan 1" through enlarging the overall diameters results in declined motions and mooring forces. Thus, this study provides the first indications towards a systemic evaluation of the dependencies of different structural parts of a submersible steel-frame offshore fish farm for hydrodynamics.

Keywords:

Hydrodynamics; CFD; Dynamic response; Offshore fish-farming; Waves

[*]Corresponding author, huangly@ouc.edu.cn

1 Introduction

The tendency of aquaculture sites moving towards the open ocean is inevitable due to the high density of nearshore aquaculture facilities and rising pollution issues Grigorakis and Rigos (2011). As the most promising solution, the development of large-scale and automatised offshore fish farms has drawn attention in recent years despite the risks of being exposed to harsh sea conditions. Typical designs are semi-submersible and submerged structures Chu et al. (2020). Circular fish farms include the semi-submersible "Ocean Farm 1" in Frohavet, Norway (Fig. 1(a)), the submersible fish farm "ShenLan 1" in the Yellow Sea Cold Water Mass (YSCWM) (Fig. 1(b)), China, the upcoming offshore fish farm developed by MariCulture AS (Fig. 1(c)), and the De-Maas spar-type fish farm deployed in the South China Sea (Fig. 1(d)). The pre-design or optimisation process of these circular structures requires fundamental knowledge about the correlation between hydrodynamic characteristics and structural features. A distinctive difference between offshore fish farms and platforms lies in the net system, which encounters the severe and oscillatory loads from waves and currents in open ocean regions. The unexpected damage issues of nets and the safe co-operations with frames in offshore fish farms need to be further clarified from the perspective of hydrodynamics.

(a) "Ocean Farm 1" Berge (2020)

(b) "ShenLan 1" (shot by Rizhao Wanzefeng Fishery Co-operation)

(c) The offshore fish-farming facility developed by MariCulture AS Drønen (2019)

(d) De Maas's semi-submersible spar-type fish farm Mutter (2020)

Figure 1: Circular offshore fish farm structures used in today's aquaculture industry.

Postprint, published in Ocean Engineering, doi:https://doi.org/10.1016/j.oceaneng.2022.111528

The hydrodynamic characteristics of offshore fish farms in waves can be investigated using flexible and efficient numerical simulations relying on linear potential theory or Computational Fluid Dynamics (CFD) and physical experiments. The numerical study on the vessel-shaped fish farm "Havfarm" is presented initially by Li et al. (2018, 2019) using wave loads based on linear potential theory and a metamodeling strategy. The screen force model Løland (1991) is applied to predict the hydrodynamics loads on nets, while linear potential theory is used to simulate the rigid body motion in waves. The dynamic response of the farm and mooring systems are evaluated in various wave conditions through the Kriging meta-model, but no physical validation is provided. An experimental investigation of the hydrodynamic response of the circular "Ocean Farm 1" in waves is investigated by Zhao et al. (2019). Here, motion responses and mooring tension forces are presented for different draughts and wave parameters. As a continuation of this work, the relevant numerical studies based on a boundary element method (BEM) and potential flow theory are presented in Liu et al. (2020). Due to the linearity of the numerical method, non-linear interactions could not be accounted for. Also, the influences of different structural features on the hydrodynamic loads are not investigated. The shielding effect of side- and bottom-net sheets are highlighted in Zhao et al. (2021); Liu et al. (2021) for "Ocean Farm 1". The momentum loss behind and hydrodynamic drag on the nets are analysed by adding a source term based on a porous medium approximation to the fluid solver. But, the effects of the relative motion between the fish farm and the viscous fluids are neglected, and the turbulence distributions around structures were not analysed. Similarly, experimental and numerical research of a semi-submersible circular fish farm is provided by Miao et al. (2021). They studied the hydrodynamic response of the structure for different wave parameters, draughts, and net solidities. The inviscid potential flow theory and a screen force model Kristiansen and Faltinsen (2012) are applied to calculate the loads on the frame and net sheets. Moreover, an experimental investigation of the hydrodynamics of a semi-submersible vessel-type fish farm has been presented in Huang et al. (2020), but the related numerical modelling misses a structural investigation due to the difficulties of modelling the slender braces. The motion responses, horizontal drifting forces, and mooring loads of the "Ocean Farm 1" model are studied physically and numerically in waves and currents Jin et al. (2021). A frequency-domain analysis covering broadband of wave frequencies is utilised, and Morison force coefficients are calibrated to predict the viscous effects on nets. The non-linear vertical accelerations and the dependences on the net damping are discussed further by Yu et al. (2021). Here, the interaction between extreme wave conditions and aquaculture fish farms is highlighted.

The investigated prototype in the present study, "ShenLan 1", has been put into production in the YSCWM region and represents the largest circular offshore fish farm in China. Equipped with two cylindrical liquid/gas tanks, the draught of "ShenLan 1" can be controlled based on the water temperature or specific operating patterns. Thus, cold-water fishes such as Atlantic salmon and Oncorhynchus mykiss can be farmed in a suitable water layer. The outline profile is an octagonal columned structure with an Ultra-High Molecular Weight Polyethylene (UHMWP) square net system and a four-point pre-tensioned mooring system. The operation site is about 130 miles off the coast, and the practical working state corresponds to a draught of 32 m. The main steel frame is the fundamental structure withstanding severe environmental loads and keeping the net volume constant. Although the hydrodynamic characteristics of "Ocean Farm 1" have been investigated extensively, the results cannot be applied to "ShenLan 1" due to a significantly different structural design. Further, the utilisa-

tion of net sheets on the top of "ShenLan 1" indicates a critical fluid-structure interaction in wave crest situations Wang et al. (2021) which is not present for "Ocean Farm 1". Here, the non-linear wave-structure interaction plays an important role especially for systems deployed in severe offshore environments. The first numerical model accounting for these interactions was presented by Martin et al. (2020) using a CFD fluid solver and a novel continuous direct forcing approach for coupling three-dimensional floating bodies with a net solver. Two classical offshore fish farms, circular and vessel-type structures, were investigated in regular and irregular waves. The dependencies of various structural features and wave parameters on the hydrodynamics of the complete farm were however not addressed.

The present study aims at filling this gap by investigating the influence of wave parameters and structural variations on the hydrodynamics of "ShenLan 1" in regular waves using the fluid-structure interaction solver in Martin et al. (2020). Multiple validation cases for the rigid body motion of a circular floater and a fish farm model in a numerical wave tank (NWT) are presented to ensure grid independence. Here, a recently developed screen force model Wang et al. (2022); Martin et al. (2022) with improved drag force prediction is included and compared with a standard screen force model Kristiansen and Faltinsen (2012) for predicting hydrodynamic loads on rigid net panels. Finally, the effects of regular wave parameters, net solidities, the draught, and the aspect ratio (AR) of the farm on the motion response, forces, and maximum mooring tension forces are discussed. Here, AR refers to the ratio between the overall diameter and height of the structure. This measure is particularly important due to the correlation with the behaviour of general floating bodies Mayilvahanan and Selvam (2011).

The structure of this work is arranged as follows: Sections 2.1, 2.2 and 2.3 introduce the fluid dynamics, rigid body motion and net solvers as well as the coupling algorithm between them. Section 2.4 describes the numerical setup including the computational domain and grids. Then, the validation of the numerical model is given in section 3. Section 4 presents the influence of the wave parameters (section 4.1), net sheets (section 4.2), draughts (section 4.3) and AR (section 4.4) on the hydrodynamics of the "ShenLan 1" fish farm. Final remarks are provided in section 5.

2 Numerical model

2.1 Fluid dynamics model

Within the framework of REEF3D Bihs et al. (2016), the mass and momentum of the fluid in the NWT are conserved by solving the continuity and Navier-Stokes (N-S) equations in the convective form

$$\begin{aligned} \nabla \cdot \mathbf{u} &= 0, \\ \frac{\partial \mathbf{u}}{\partial t} + \mathbf{u} \cdot \nabla \mathbf{u} &= -\frac{1}{\rho} \nabla p + \nu \left[\nabla^2 \mathbf{u} + \nabla \left(\nabla \cdot \mathbf{u} \right) \right] + \mathbf{S}. \end{aligned} \tag{1}$$

Here, $\mathbf{u}$ is the velocity vector, ρ is the fluid density, p denotes the pressure, and $\mathbf{S}$ represents the external source term composed of the gravity vector $\mathbf{g}$ and the forcing terms $\mathbf{f_n}$ for the

nets and $\mathbf{f_b}$ for the floating rigid body. Further, ν denotes the kinematic and turbulent eddy viscosity accounting for the turbulence effects around the free surface. Here, a $k-\omega$ turbulence model Bihs et al. (2016) is applied. Two-phase flow is enabled by capturing the interface between the air and water phases implicitly using the zero level set of a smooth signed distance function Φ Osher and Sethian (1988); Bihs et al. (2016). The level set method includes solving the advection equation for Φ with a reinitialization procedure after the transport of the free surface. The high-fidelity and flexible free-surface modelling in REEF3D have been previously verified in the breaking wave and focused wave cases Aggarwal et al. (2019); Cui et al. (2021). The density and viscosity at any location of the domain are then given as

$$\begin{aligned} \rho &= \rho_w H(\Phi) + \rho_a (1 - H(\Phi)), \\ \nu &= \nu_w H(\Phi) + \nu_a (1 - H(\Phi)), \end{aligned} \tag{2}$$

with w indicating water, a indicating air and $H(\Phi)$ denoting the smoothed Heaviside step function

$$H(\Phi) = \begin{cases} 0 & \text{if } \Phi < -\epsilon, \\ \frac{1}{2}\left(1 + \frac{\Phi}{\epsilon} + \frac{1}{\pi}\sin\left(\frac{\pi\Phi}{\epsilon}\right)\right) & \text{if } |\Phi| \leq \epsilon, \\ 1 & \text{if } \Phi > \epsilon, \end{cases} \tag{3}$$

with $\epsilon = 2.1\Delta x$ and the characteristic length Δx ensuring the smooth transition between water and air.

A finite difference method and a staggered grid are employed, ensuring a tight coupling between the pressure stored in the cell centres and the velocities calculated at cell faces. The fifth-order Weighted Essentially Non-Oscillatory (WENO) scheme Jiang and Shu (1996) is used for the spatial discretisation of the convection term in Eq. (1), and a Hamilton-Jacobi version Jiang and Peng (2000) is utilised for the advection equation of the level set method. The diffusion term is discretised with the second-order accurate central difference scheme. The explicit third-order total variation diminishing (TVD) Runge-Kutta method Shu and Osher (1988) is utilised for the time advancement of the convective and source terms, while the diffusion term is treated implicitly using an Euler method Bihs et al. (2016). The pressure and velocities of the new time step are calculated following a projection method Timmermans et al. (1996): in each k-th sub-step of the third-order Runge-Kutta scheme, an intermediated velocity u^* is predicted using the pressure gradient of the previous step $i-1$:

$$\frac{\mathbf{u}^* - \beta_i \mathbf{u}^{(n)}}{\alpha_i \Delta t} = \frac{1}{\Delta t}\mathbf{u}^{(i-1)} - \mathbf{u}^{(i-1)} \cdot \nabla \mathbf{u}^{(i-1)} - \frac{1}{\rho}\nabla p^{(i-1)} + \frac{1}{\alpha_i}\nu \left[\nabla^2 \mathbf{u} + \nabla\left(\nabla \cdot \mathbf{u}\right)\right]^* + \mathbf{S}^*, \tag{4}$$

with $\alpha_i = 1.0, 1/4, 2/3$, $\beta_i = 0, 3/4, 1/3$ and $i = 1, 2, 3$. Then, a temporary pressure correction term p_{co} is obtained from the Poisson equation

$$\nabla \cdot \left(\frac{1}{\rho}\nabla p_{co}\right) = \frac{1}{\alpha_i \Delta t}\nabla \cdot \mathbf{u}^*. \tag{5}$$

This Poisson equation is solved using a multigrid preconditioned BiCGStab solver from the HYPRE library van der Vorst (1992). Finally, the corrected pressure and divergence-free velocity fields are expressed as

$$
\begin{aligned}
p^{(i)} &= p^{(i-1)} + p_{co} - \rho\nu\nabla\cdot\mathbf{u}^*, \\
\mathbf{u}^{(i)} &= \mathbf{u}^* - \frac{1}{\rho}\alpha_k\Delta t\nabla p^{(i)}.
\end{aligned} \tag{6}
$$

2.2 Moored floating body motion solver

The floating rigid body motion and its coupling to the viscous fluid solution are calculated through the continuous direct forcing approach as presented in Martin et al. (2020). Here, the fluid and solid phases are distinguished using a level set function from the bodies' geometry. The correct boundary conditions are enforced by including a forcing term into the system after obtaining $\mathbf{u}^{(*)}$ in Eq. (4) without the source term. As shown by Martin et al. (2020), this term is given as

$$
\mathbf{f}_\mathbf{b}^{(*)} = H(\Phi_s^{(*)})\cdot\left(\frac{\mathbf{J}(\mathbf{u}^{(*)}) - \mathbf{u}^{(*)}}{a_i\Delta t}\right), \tag{7}
$$

where $H(\Phi_s)$ represents a smoothed Heaviside step function as written in Eq. (3), and $\mathbf{J}(\mathbf{u}^*)$ denotes the rigid velocity field projection operator which projects the velocity field into a divergence-free rigid body velocity field. It is defined in the Euler coordinate system as

$$
\mathbf{J}(\mathbf{u}^*) = \dot{\mathbf{X}} + \omega\times\mathbf{r}, \tag{8}
$$

with $\mathbf{X}$ and ω the translational and rotational velocity fields of the floating body, respectively, and $\mathbf{r}$ the distance between the cell centres and the centre of gravity of the floating object. The six degrees-of-freedom (DOF) motions of the rigid body are obtained from solving Newton's second law and the rotational momentum equations using the quaternion representation described in Martin et al. (2021). The forces and moments acting on the floating body are calculated based on the integration over the triangulated body surface with N triangles:

$$
\begin{aligned}
F_x &= \sum_{i=1}^{N}(-\mathbf{n}p + \rho\nu\mathbf{n}\tau)_i\cdot\Delta\Omega_i, \\
M_x &= \sum_{i=1}^{N}\mathbf{r}_i\times(-\mathbf{n}p + \rho\nu\mathbf{n}\tau)_i\cdot\Delta\Omega_i.
\end{aligned} \tag{9}
$$

Here, $\mathbf{n}$ is the surface normal vector, τ is the stress tensor, and $\mathbf{r}$ denotes the distance vector from each element to the centre of gravity. It is referred to Martin et al. (2020) for more details.

Steel catenary chains are adopted as the mooring system of the offshore fish farm. The restoring forces from the heavy catenary keep the structure in equilibrium in wave fields. In

this study, the catenary solution is found analytically as given in Faltinsen (1993) for elastic material. The bending stiffness in this solution is not considered due to the large curvature of the chains. As shown in Eq. (10), the tensions can be calculated once the position of the fairlead and anchor points are given:

$$
\begin{aligned}
h &= \frac{T_H}{w}\left[\frac{1}{\cos\phi_w} - 1\right] + \frac{1}{2}\frac{w}{EA}l_s^2, \\
x &= \frac{T_H}{w}\log\left(\frac{\sqrt{(T_H^2 + T_Z^2)} + T_Z}{T_H}\right) + \frac{T_H}{EA}l_s.
\end{aligned} \tag{10}
$$

Here, x and h denote the horizontal and vertical distances between the fairlead and anchor points, respectively. T_H and T_V are the horizontal and vertical components of tensions, ϕ_w represents the angle formed by the mooring tension, T_H is the direction vector, w corresponds to the constant weight per unit mooring line length in the water, EA is the elastic stiffness, and l_s denotes the length of the mooring line. Since the relative motion of the mooring system is neglected, the influence of the fluid hydrodynamics is ignored as it is considered to be small in the investigated cases. In order to achieve two-way coupling with the rigid body motion solver, the restoring tension forces from the chains are transmitted as external forces to the rigid body solver in order to restrict the translational and rotational motion of the complete system.

2.3 Modelling the forces on the net and its coupling to the fluid solver

The nets are assumed to be rigid because they are restricted in motion and tightly attached to the columns of the structure using pre-tightened ropes. The net sheets are attached to the thick columns of the frame system as illustrated in Fig. 2(a). This implies minor deformations of the nets so that the deformation can be overlooked. But, the hydrodynamic loads on the nets as well as the influence of nets on the velocity field are crucial which require a two-way coupling between the various solvers. A weakly coupled strategy is chosen by adding the hydrodynamical and inertial forces of the net as additional body forces to the rigid body dynamic solvers.

A surrogate model has to be incorporated to calculate the forces on the net due to the computational costs required to simulate the flow around each twine. Here, the screen force model is typically used in previous research involving fluid-nets interactions Kristiansen and Faltinsen (2015); Yao et al. (2016); Shen et al. (2018); Martin et al. (2020). This approach was extended to time-dependent cases by Martin and Bihs (2021), which is used in this study. Therefore, the total loads on the nets are determined by summing up the loads on smaller surface elements discretising the net surface. The most important contribution is due to the drag (F_d) and lift (F_l) forces as presented in Fig. 2(b). They are calculated from the force vector and the normal ($\mathbf{n_d}$) and tangential ($\mathbf{n_l}$) directions of the relative velocity ($u_{rel,s}$) for each macro screen element E_s with outline area A_s:

$$
F_{hydro} = \sum_{s=1}^{E_s} \frac{\rho}{2} A_s u_{rel,s}^2 (C_d \mathbf{n_d} + C_l \mathbf{n_l})_s. \tag{11}
$$

The constants C_d and C_l denote the drag and lift force coefficients and are often determined as functions of the net solidity (S_n), Reynolds number (Re) and angle of attack (θ) Aarsnes et al. (1990); Løland (1991); Kristiansen and Faltinsen (2012). However, the usage of the above three parameters predicting the hydrodynamic loads fails for nets with the same solidity but varying twine diameters and lengths Wang et al. (2022). Besides, the dependencies of the coefficients have to be expressed in terms of regression formulae using experimental data Kristiansen and Faltinsen (2012); Yao et al. (2016); Martin et al. (2020) or theoretical derivations Aarsnes et al. (1990); Løland (1991). The applicability of these formulae is thus restricted to a small range of twine configurations and materials.

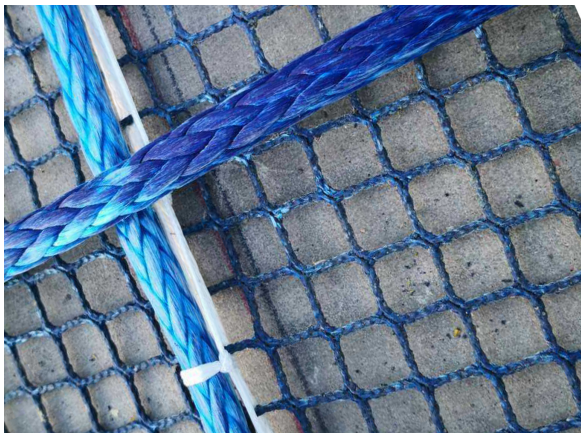

(a)

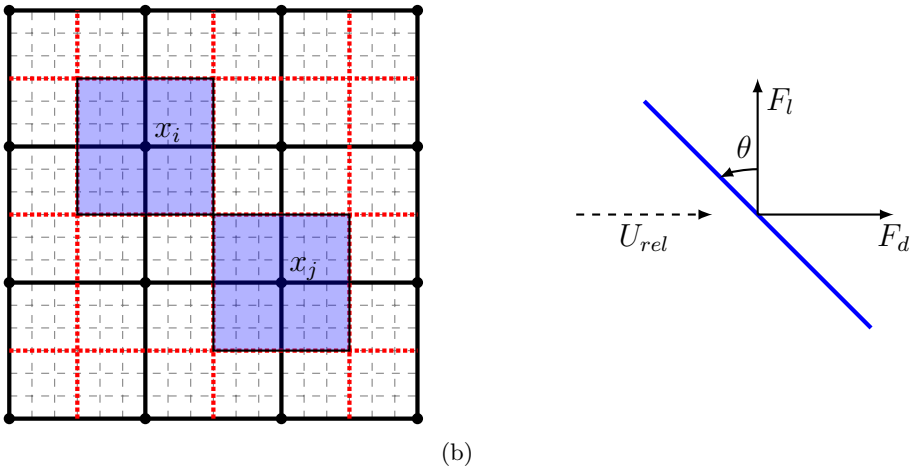

(b)

Figure 2: Overview of the net sheets used for the "ShenLan 1" fish farm (a) and the equivalent screen force representation (b).

The capabilities of the screen force model are improved by incorporating the independent variables u_{rel} as well as the diameter (d) and length of the twines (l) to calculate the force coefficients. This choice is justified by their importance to calculate the fundamental parameters S_n and Re. Following this idea, a novel simulation-based screen force model Wang et al. (2022) is introduced using high-resolution $k-\omega$ SST-Improved delayed detached eddy

simulations of a small segment of the full-scale twisted fabric net panel for various θ. Nonlinear relations combining $\theta = 0^\circ \sim 90^\circ$ are formulated using a metamodeling approach and polynomial fittings in Martin et al. (2022). The resulting formulae are given as

$$\begin{aligned} C_d &= C_{d,\theta=90^\circ} + a\theta + b\theta^2, \\ C_l &= c\theta + d\theta^2, \end{aligned} \tag{12}$$

$$\begin{aligned} a &= 0.044(C_{d,\theta=45^\circ} - C_{d,\theta=90^\circ}) + 0.0111 C_{d,\theta=90^\circ}, \\ b &= -0.0004938(C_{d,\theta=45^\circ} - C_{d,\theta=90^\circ}) - 0.0002469 C_{d,\theta=90^\circ}, \\ c &= 0.044 C_{l,\theta=45^\circ}, \\ d &= -0.0004938 C_{l,\theta=45^\circ}. \end{aligned} \tag{13}$$

The coefficients $C_{d,\theta=90^\circ}$, $C_{d,\theta=45^\circ}$ and $C_{l,\theta=45^\circ}$ are given in A. The validation and comparison to other screen force models for net panels in current and waves scenarios is presented below in order to highlight its advantages.

Finally, the coupling between the rigid net model and the fluid solver is performed as proposed by Martin et al. (2020). Following the law of momentum balance, the velocity reduction behind net panels can be approximated as the momentum loss of the fluid due to the presence of the net. A source term $\mathbf{f_n}$ can be calculated and added to Eq. (1). It is calculated at each cell point $\mathbf{x}_i$ using the interpolation

$$\begin{aligned} \mathbf{f_n}(\mathbf{x_i}) &= \sum_{L=1}^{L_i} \frac{\mathbf{f}(\mathbf{x}_L)}{\Delta x \Delta y \Delta z} \, \mathrm{D}\left(\frac{x_i - x_L}{\Delta x}\right) \, \mathrm{D}\left(\frac{y_i - y_L}{\Delta y}\right) \, \mathrm{D}\left(\frac{z_i - z_L}{\Delta z}\right), \\ \mathbf{f}(\mathbf{x}_L) &= \left[F_{hydro} + F_{inertial} + F_G + F_B\right]_L . \end{aligned} \tag{14}$$

Here, L_i represents the number of Lagrangian points placed on the net panel within a defined kernel D around $\mathbf{x}_i$. Further, $F_{inertial}$ represents the inertial forces due to the relative motions between fluid and net twines and added mass effects, F_G represents the gravitational force and F_B denotes buoyancy forces (see Martin and Bihs (2021) for details).

2.4 Numerical setup

A geometrical similarity ratio due to the Froude number of 1:60 is utilised for the submersible structure as well as mooring cables. One should notice that the model-scale study instead of a full-scale one is carried out, as the computational grids used for simulations are determined through a model-scale floater experiment as well as model-scale fish farm experiments in Section 3. The grid-independence study in validations ensures the accuracies of CFD modelling. Although the scaling effects can be avoided, the influence of grids resolution at full-scale CFD simulations should be investigated further Koop and Bereznitski (2011); Schmitt and Elsäßer (2017). Based on the offshore engineering practice, the choice of 1:60 is reasonable since the scaling ratio is not smaller than 1:100, then the scale effects are negligible in heave and pitch motions Wei et al. (2015); Palm et al. (2018). In a deeper sight, the viscous effects of fluids are dominated by Re, which does not scale with Froude scaling laws, Re of model-scale braces in this study are however in the sub-critical or critical regions, thus the effects of Re

on hydrodynamic loadings on the structures can be minimised. The wave parameters are also specified using the Froude scaling of the actual sea state. As analysed in Faltinsen and Shen (2018); Zhao et al. (2019), a uniform geometrical scaling is not feasible for the net system of offshore fish farms since the dimensions and elastic properties of the twines are relatively small in full-scale facilities. The scaling of the twine dimensions can thus affect the predictions of the hydrodynamic forces. Therefore, the net parts are not scaled Jin et al. (2021); Wang et al. (2021). The structural dimensions of the "ShenLan 1" offshore farm with the mooring cable are depicted in Fig. 3(a) and Tab. 1 in production condition. The four-point mooring system consists of chains connecting the fairleads (at both bottoms of two air & liquids tanks with F1 - F4 in Fig. 3(a)) with mounting points in the seabed, and each cable is configured orthogonal and symmetrical to each other.

Table 1: The structural dimensions of the "ShenLan 1" fish farm with the mooring system in the production condition. The subscripts p and m denote the prototype and model scale.

Parts	**Components**	**Dimension**	**Unit**	**Scaling**	**Data**$_m$	**Data**$_p$
Frames	Overall diameter CL	Length	[m]	λ	1.01	60.42
	Overall height CH	Length	[m]	λ	0.57	34.44
	Central column	Length	[m]	λ	0.58	34.62
		Diameter			0.06	3.48
	Outer upper columns	Length	[m]	λ	0.25	15.06
		Diameter			0.03	1.98
	Outer upper columns	Length	[m]	λ	0.22	12.90
		Diameter			0.05	3.00
	Horizontal brace	Diameter	[m]	λ	0.02	1.02
	Nets sheets	Bar length	[m]	1	0.02	0.02
		Bar diameter	[mm]	1	3.00	3.00
		Solidity ratio	[-]	1	27.75%	27.75%
	Weight	Mass	[Kg]	λ^3	15.90	3.43×10^6
		Net mass	[Kg]	λ^3	6.45	1.39×10^6
Mooring cables	Total length L_m	Length	[m]	λ	8.51	510.40
	Diameter d_m	Length	[m]	λ	0.03×10^{-1}	0.18
	Weight in air γ_m	Mass	[Kg/m]	λ^2	4.65×10^{-2}	167.29
	Cable density ρ_m	Density	[Kg/m^3]	1	7.85×10^3	7.85×10^3
	Axial elasticity EA	Elastic modulus × cross-sectional area	[N]	λ^3	3274.06	7.07×10^8
Draughts	Overhauling	Depth	[m]	λ	0.19	11.40
	Net-drying				0.38	22.80
	Production				0.53	31.80

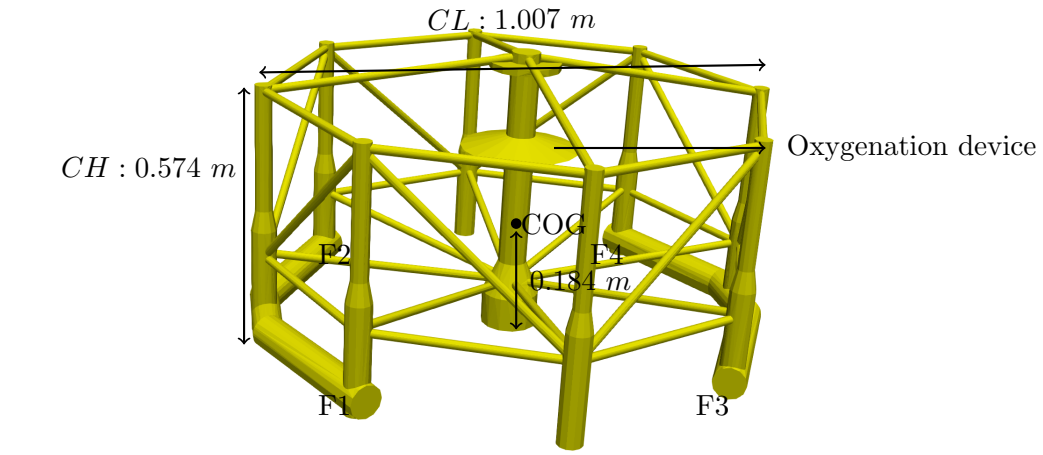

(a)

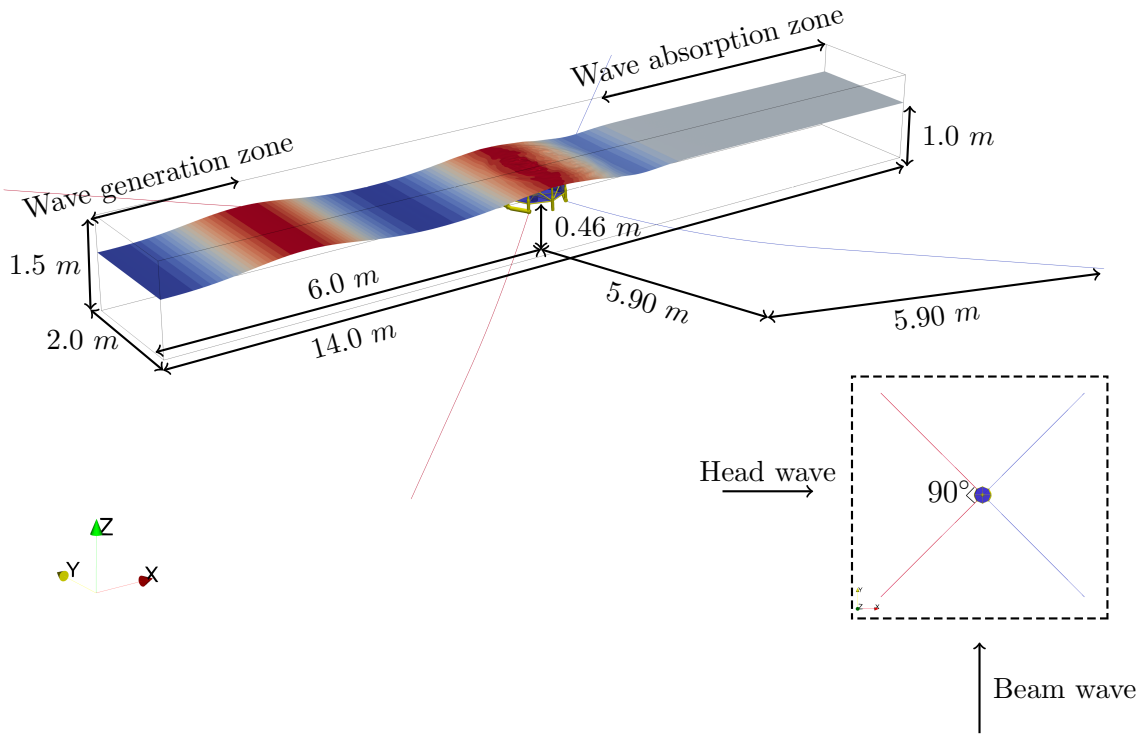

(b)

Figure 3: The frame structure (a) of the model-scaled fish farm, and the computational domain as well as the mooring system for the "ShenLan 1" offshore farm (b).

The fish farm model is placed in a 14.0 m × 2.0 m × 1.5 m NWT, with a 6.0 m distance to the left boundary and 1.0 m water depth (see also Fig. 3(b)). Eventual boundary effects are omitted as the width is larger than the physical flume tank used for the experiments on

the "Ocean Farm 1" model Zhao et al. (2019) and symmetry boundary conditions are used. One should notice that the lower components of the modelled cables are placed outside the computational domain in order to reduce the domain size. This is justified as the interaction with the fluid is neglected anyway. Also, the flow velocities close to the tank bottom are small and a large portion of the mooring cables lie on the ground Martin and Bihs (2021). The generation of second-order Stokes waves is achieved by the relaxation method Jacobsen et al. (2012), while an absorption zone with a length of two wavelengths (L) is used at the end of the tank to avoid wave reflections. The accuracy of the wave generation and propagation has been previously validated for floating bodies in the REEF3D framework Bihs and Kamath (2017); Martin et al. (2020). As shown in Tab. 2, 15 wave cases are considered. They include regular waves with the wave heights (H) 0.06 m, 0.10 m and 0.18 m, the wave periods (T) of 1.2 s, 1.4 s, 1.6 s and 1.8 s as well as the wave-incoming directions 0° - 180°. Fig. 3(b) refers to the case corresponding to 0° wave-incoming direction, so-called the head wave scenario. The setup corresponds to the practical recorded sea states in the YSCWM Yao et al. (1992), following the Froude scaling. The computational grid is shown in Fig. 4. A uniformly-sized refinement zone is placed around the structure, and the cell sizes outside the inner zones increase gradually with a linear stretching factor of 1.03 until a maximum cell size of 0.02 m is achieved. The cell size in the refinement region is determined from free decay tests presented in section 3.1.

Table 2: The cases setup for studying the dependencies of wave parameters on the hydrodynamics of the fish farm model

Wave cases	**H [m]**	**T [s]**	**Frequency [Hz]**	**Steepness**	**Direction**
W1	0.06			0.08	
W2	0.10	1.20	0.83	0.14	
W3	0.18			0.25	
W4	0.06			0.06	
W5	0.10	1.40	0.71	0.11	
W6	0.18			0.19	0° (head wave),
W7	0.06			0.05	180°
W8	0.10	1.60	0.63	0.08	
W9	0.18			0.15	
W10	0.06			0.04	
W11	0.10	1.80	0.56	0.07	
W12	0.18			0.13	
W13					45°
W14	1.80	1.80	0.56	0.13	90° (beam wave)
W15					135°

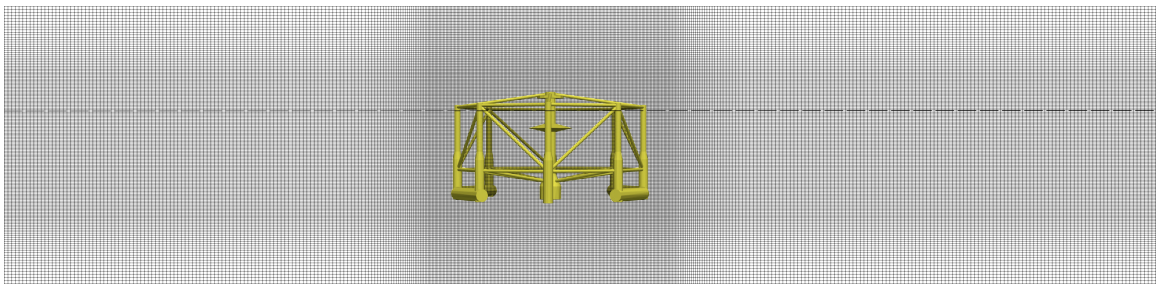

Figure 4: Computational grid for the simulation of the "ShenLan 1" fish farm in waves. The dotted line represents the initial free surface location in the numerical domain.

3 Validations of the numerical method

3.1 Validation of the rigid body motion solver

First, the accuracy of the rigid body motion solver is validated against the free decay measurement of a vertical cylindrical floater reported in Moura Paredes et al. (2016); Palm et al. (2016). Here, a 35.85 kg floater with a diameter of 0.515 m and a height of 0.401 m is placed vertically in a 0.9 m deep tank (Fig. 5). The floater has an initial draft of 0.172 m. The centre of gravity (COG) is located 0.075 m above the bottom surface, and the moments of inertia around the COG are $I_{xx} = I_{yy} = 0.90$ kg·m^2, I_{zz}= 1.18 kg·m^2. A heave decay test in a 0.9 m deep tank with an initial displacement of 0.075 m is executed to examine the grid convergence. Five grid point distances with uniform cell sizes between 0.005 m and 0.05 m are considered. Fig. 6(a) shows the comparison of the time series for the heave motion between the simulation and experimental measurements. It can be noted that the coarsest mesh case presents a distinct phase deviation from the experimental data after the second peak, while the grid refinement improves the results. Additionally, some under-estimation is visible for coarse grids which can again be diminished using further refinement levels. The cases with cell sizes smaller than 0.0075 m have captured most peaks, troughs and frequencies with differences below 15%. Thus, the inner refinement region is set to have cell sizes of 0.0075 m for the subsequent investigations.

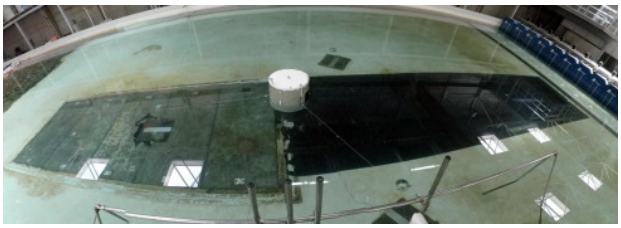

Figure 5: The cylindrical floater experimental case Moura Paredes et al. (2016); Palm et al. (2016) used for the validation of the rigid motion solver.

The convergence for diminishing Courant numbers is depicted in Fig. 6(b). The definition of Courant number refers to $U_0\Delta t/\Delta x$, where U_0 represents the flow velocity, Δt is the time step within the simulation while Δx is the characteristic size of the mesh cell. It incorporates

the stability of the time discretisation scheme and the computational efficiency. In REEF3D, the adaptive time-stepping strategy is used to control the Courant number and takes the influence from velocity, diffusion and the source term Griebel et al. (1998); Bihs et al. (2016). From Fig. 6(b), It can be seen that no evident difference amongst the three heave motions is present for the optimised grid size from above. As a result, all simulations in this paper are conducted using a Courant number of 0.3. Finally, the chosen setup is applied to a free pitch decay test (Fig. 6(c)). Here, the COG is moved to 0.0788 m, while the moment of inertia is increased by 0.05 kg·m^2. It is reported in Paredes et al. (2015) that the experimental uncertainties of the moment of inertia, centre of gravity and draft related to the buoy properties lead to the adjustments, which is further confirmed in Palm et al. (2016).

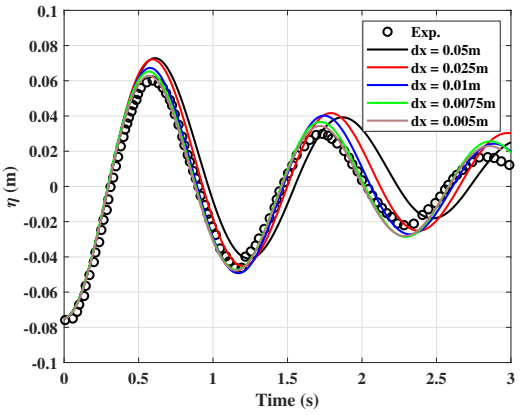

(a) Free heave decay motion

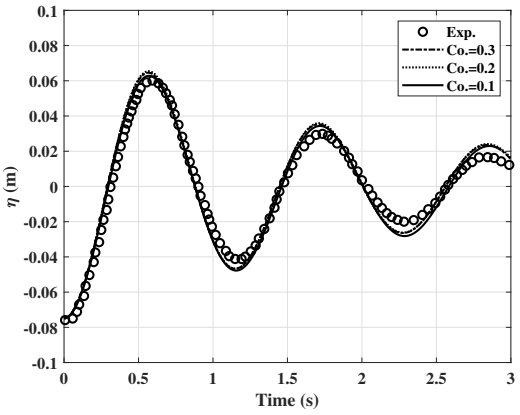

(b) Courant number dependency for the free heave decay with a cell size of 0.0075 m.

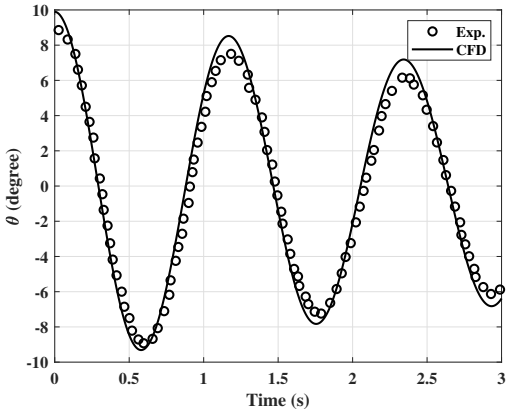

(c) Free pitch decay motion

Figure 6: Validation of the free decay motions of a vertical cylindrical floater. The experimental data is taken from Moura Paredes et al. (2016); Palm et al. (2016).

3.2 Validation of the net hydrodynamics solver

The accuracy of the prediction of the hydrodynamic loads on stiff net sheets in waves and currents is assessed using a comparison to experimental data and the improved properties of the simulation-based screen force model (SSM). For comparison, the classical screen force model approach (CSM) Kristiansen and Faltinsen (2012) is shown.

First, the hydrodynamic drag and lift forces together with the velocity reduction are extracted for different net cases in current Bi et al. (2013); Føre et al. (2021) with varying solidities, Re and θ. The dimension of the computational domain is defined as 10.0 m×4.0 m×3.0 m (length×width×height) for all cases. Thereby, no interference from the tank walls is expected because the domain is at least three times larger than the width of the panel Tsukrov et al. (2011). As can be seen from Tab. 3, the deviations for the drag and lift forces simulated using SSM are smaller than by using CSM which over-predicts certain configurations by up to 40.54%. Except for the lift component of N2, the numerical results obtained by SSM are below 7% from the experimental data. In contrast, the results using CSM deviate consistently by more than 10%. In terms of the fluid velocity reduction after passing the net panels, the performances of the two screen models are similar as the relative discrepancy fluctuates between 4% and 7%.

Table 3: Numerical and experimental hydrodynamic loads on and velocity reductions $\overline{V_r}$ behind net panels in current. $\overline{F_D}$ and $\overline{F_L}$ represent time-averaged drag and lift forces. $\overline{V_r}$ is defined as the ratio between the mean streamwise velocity behind the panel and the incoming velocity. SSM corresponds to the simulation-based screen force model Martin et al. (2022), while CSM is the classical screen force model Kristiansen and Faltinsen (2012) as implemented in Martin et al. (2020). The relative differences RD are defined as $(\overline{F_D} - \overline{F_D}^{exp})/\overline{F_D}^{exp} \cdot 100\%$.

Net cases	$\boldsymbol{\theta}$	$\boldsymbol{Re}$	$\boldsymbol{S_n}$		**SSM**	**CSM**	**Exp.**
N1 in Føre et al. (2021)	90°	1680.7	0.23	$\overline{F_D}$ (N)	195.75	219.72	195.92
				RD	-0.09%	12.15%	-
				$\overline{V_r}$ (-)	88.83 %	87.58%	83.72%
				RD	6.10%	4.61%	-
N2 in Føre et al. (2021)	67.5°	1680.7	0.23	$\overline{F_D}$ (N)	166.87	196.13	171.43
				RD	-2.66%	14.41%	-
				$\overline{F_L}$ (N)	27.42	51.62	36.73
				RD	-25.35%	40.54%	-
N3 in Bi et al. (2013)	90°	493.8	0.24	$\overline{V_r}$ (-)	86.14%	84.34%	91.10%
				RD	-5.44%	-7.42%	-

Next, the time series of the horizontal loads on a rigid net in regular waves are evaluated against the experimental measurements of two net-panel cases in Dong et al. (2020). The structural information of N4 and N5 cases and the tested waves are summarised in Tab. 4. The panels are fixed in a frame of 0.5 m×0.5 m beneath the 10 cm of the water level, then placed in a 3 m deep wave tank. By plotting the surface elevations at two wave gauges (Fig. 7(a) 7(c)), it can be seen that the numerical model generates the expected waves with less than 5% damping. Both screen force models qualitatively follow the oscillating envelopes of the time-series forces. SSM captures most peaks and troughs, whereas CSM over-predicts the magnitudes of drag forces which is in accordance with the former results.

Table 4: Cases used to simulate a rigid net panel in waves. More detailed information about the tested panels can be found in Dong et al. (2020)

Net cases	θ	S_n	H [cm]	T [s]
N4	90°	0.168	7.2	2.5
N5			10.8	

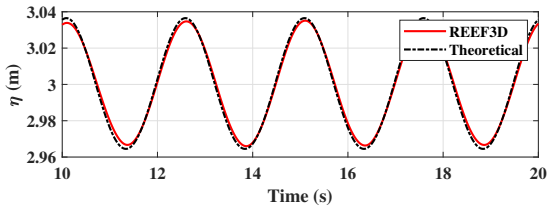

(a) Surface elevation at the wave gauge for N4

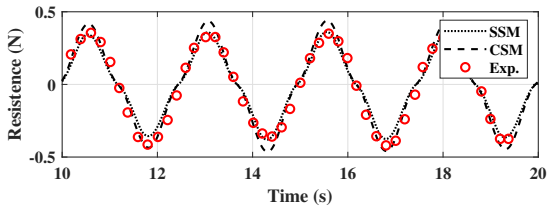

(b) Drag forces at N4

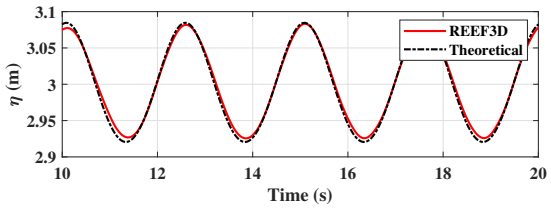

(c) Surface elevation at the wave gauge for N5

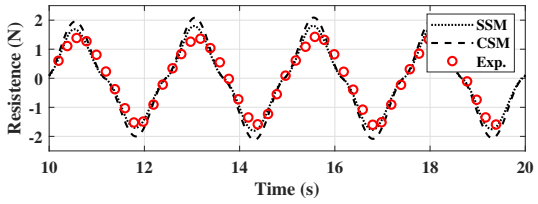

(d) Drag forces at N5

Figure 7: Numerical and experimental time series of the surface elevation and horizontal forces for the rigid panel in waves. The experimental data is taken from Dong et al. (2020).

3.3 Validation of the hydrodynamics of a circular fish farm

The rigid body dynamics solver including catenary chains has been successfully validated for a moored floating wind turbine in Martin and Bihs (2021). Here, the coupled framework, consisting of the moored-floating body motion and the net solvers, is further tested for the semi-submersible offshore fish farm "Ocean Farm 1" using the experimental data which has been presented in Zhao et al. (2019). The flume test was conducted in a wave-current flume at the State Key Laboratory of Coastal and Offshore Engineering, Dalian University of Technology, China. The physical model (Fig. 8(a)) consists of the primary frame, net, weight, and mooring systems, of which draughts are obtained through the adjustments of the water percentage in the ballast system and the sand in the top box. The frame system is built with a geometrical scaling of 1:120 and 3:40 for the net. The 3 m mooring ropes, including 2.9 m of polyethylene rope and a 0.1 m stainless spring, are further modelled as linear elastic springs in the numerical simulations Liu et al. (2020). The investigated draught of the "Ocean Farm 1" model is 36 cm, corresponding to the actual draught during the production condition. The 10 m×2 m×1.8 m dimensions of the NWT, as well as the numerical model are presented in Fig. 8(b). The H of the regular waves in this validation is chosen as 0.10 m, while T is 1.0 s and 1.2 s, respectively. More details on the structure can be found in Zhao et al. (2019); Liu et al. (2020).

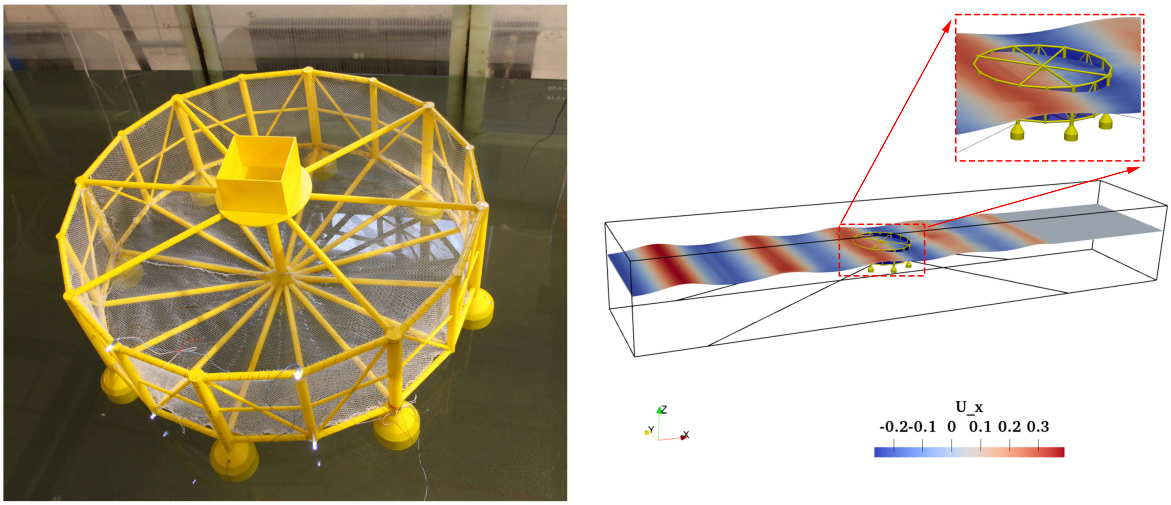

(a) Physical model Zhao et al. (2019)

(b) Numerical model in REEF3D

Figure 8: The profiles for the physical Zhao et al. (2019) and the numerical model of the semi-submersible offshore fish farm.

The resulting motion amplitudes and maximum tension forces are presented in Tab. 5. The translational and rotational motions show a deviation of less than 10% from the physical data. The predicted maximum mooring tensions on the windward-side show around 17% deviation. One possible reason for this increased deviation could be that the experimental-used polyethylene mooring ropes did not completely follow Hook's law with a constant elastic coefficient during elongation Zhao et al. (2019), thereby the accurate modelling for the mooring line through the spring treatment has been increased. Another possible explanation lies in the deviations of fairlead points between the numerical and physical models.

Table 5: Numerical and experimental motion responses and maximum mooring tension forces of the "Ocean Farm 1" model with 36 cm draught in regular waves. The motion responses are defined as two-time amplitudes in accordance with Zhao et al. (2019); Liu et al. (2020). The relative differences RD are defined as in Tab. 3.

H [m]	**T [s]**		**motion responses**			**Maximum mooring tensions**
			Heave [m]	**Surge [m]**	**Pitch [°]**	**(windward) [N]**
0.10	1.0	CFD	2.46	1.40	4.54	3.01
		Exp.	2.43	1.48	4.30	2.56
		RD	1.39%	-5.28%	5.51%	17.34%
	1.2	CFD	3.87	3.00	6.42	3.74
		Exp.	3.69	3.20	6.10	4.60
		RD	4.74%	-6.39%	5.16%	-18.81%

4 Results and discussions

In the following, the hydrodynamic characteristics of the fish farm model are investigated in waves using the linear transfer function (Response Amplitude Operator, RAO), the maximum mooring tensions, and wave loads on the structure and nets in time and frequency domains. The sampling duration for each case covers eight periods of the steady-state response. In regular waves, the RAO is then calculated using the ratio between the amplitudes of the motion responses A_m and regular waves A_w as

$$RAO = \frac{A_m}{A_w}. \tag{15}$$

The horizontal drifting and vertical loads are presented using the mean, linear and second-order harmonic components of the force amplitudes obtained from a fast Fourier transform (FFT) analysis.

The natural frequency represents the inherent nature of an oscillating system, describing the damped behaviour after an outside disturbance from the static equilibrium position Alciatore (2007). It is introduced to study the motion responses of the floating bodies with the variations of structural properties, while RAO is utilised for illustrating the relationship between motions and wave frequencies. Initially, it is assumed that the free decay motions of the moored floating bodies follow the linear equivalent damping form, so the logarithmic decrement method (LDM) can be utilised for obtaining the overall damping ratio, and natural frequency of under-damped systems Singiresu (1995). Following the procedure introduced by Çelik and Altunkaynak (2020), the logarithmic decrement magnitude can be defined using the free decay signal of the single DOF system

$$\delta = \ln(\frac{\tau_i}{\tau_{i+2}}), \tag{16}$$

where τ_i and τ_{i+2} denote the consecutive peaks with the same sign with the forwarding of free decay signals. Then the elapsed time between the above consecutive peaks T_d can be used for calculating the damped natural frequency of the system ω_d as

$$\omega_d = \frac{2\pi}{T_d}. \tag{17}$$

Finally, the undamped natural frequency ω_n of the system can be obtained combing the damping ratio ζ and Eq. (17) as

$$\begin{aligned} \zeta &= \frac{\delta}{\sqrt{4\pi^2 + \delta^2}}, \\ \omega_n &= \frac{\omega_d}{\sqrt{1-\zeta^2}}. \end{aligned} \tag{18}$$

4.1 Hydrodynamics of the fish farm model for varying wave parameters

4.1.1 motion responses

In head waves, the translational and rotational motions of the fish farm model with draught 0.53 m and different H as well as wave frequencies are shown in Fig. 9. The amplitudes of the translational and rotational motions decrease with increasing wave frequency. This is in accordance with the experimental and numerical results in Zhao et al. (2019); Liu et al. (2020); Martin et al. (2020) and indicates a minor response of the offshore aquaculture structure in high-frequency wave excitation Fredriksson et al. (2003). With the increase of H and frequencies, the surge motions show a rapid decrease, while this tendency is less significant for the heave and pitch motions. This implies that the influence of H on themotion responses is smaller than the one from wave frequency variation. Especially, a minor influence of H on the high-frequency range of the surge motion is observed. For wave cases with frequencies below 0.7 Hz, the surge motion is dominant compared to the heave and pitch motions. This is due to the longer durations of unidirectional wave loads acting on the frame. Additionally, the stiffness of the mooring system might be accounted for the surge response of semi-submersibles at lower wave frequenciesPinkster (1980).

For the case with H below 0.10 m and a frequency of 0.56 Hz, the surge motion follows the wave envelope which might result in a dangerous situation in the operated draught. Compared to the numerical findings of the "Ocean Farm 1" model in Liu et al. (2020), it is indicated that the increased velocities of the fluid particles with the increase of H cannot affect the range of expected motion amplitudes. It is also to mention that the smaller magnitudes of the heave and pitch motion could be caused by the restoring effect from the mooring system which acts rather vertically than horizontally. This finding is in contrast to the circular semi-submersible fish farm experiments in Miao et al. (2021), where a horizontal hanging spring rope system was used. Thus, a positive correlation between the motions and H could be observed. Moreover, the current configuration of mooring catenary chains results in more considerable vertical force components compared to the elastic springs used in Zhao et al. (2019); Liu et al. (2020). It is thus substantiated that using elastic ropes for mooring restrains, as done in Wang et al. (2021), contributes to increased response amplitudes compared to catenary-chain configurations as used in this study.

The effect of the wave steepness on the motion responses of the "ShenLan 1" model is not significant. In particular, no distinct motion patterns with decreasing wave steepness from 0.08 to 0.04 can be observed for the wave cases W1, W8, W11, W4, W7 and W10. This is in contrast to the response of the "Ocean Farm 1" model in Liu et al. (2020). This indicates that the motion responses are sensitive to minor geometrical variations, such as the AR, so the analysis of one circular offshore fish farm cannot be directly transferred to another. A special feature of this fish farm is the additional net on the top of the structure. This protection is necessary because the structure eventually fully submerges in waves with large H as it is shown in Fig. 10. Moreover, the impacts of wave directions on motion responses are evaluated in Fig. 11. It can be concluded that the impacts on the translational and rotational motions are minor due to the structural symmetry of the central column in the fish farm model.

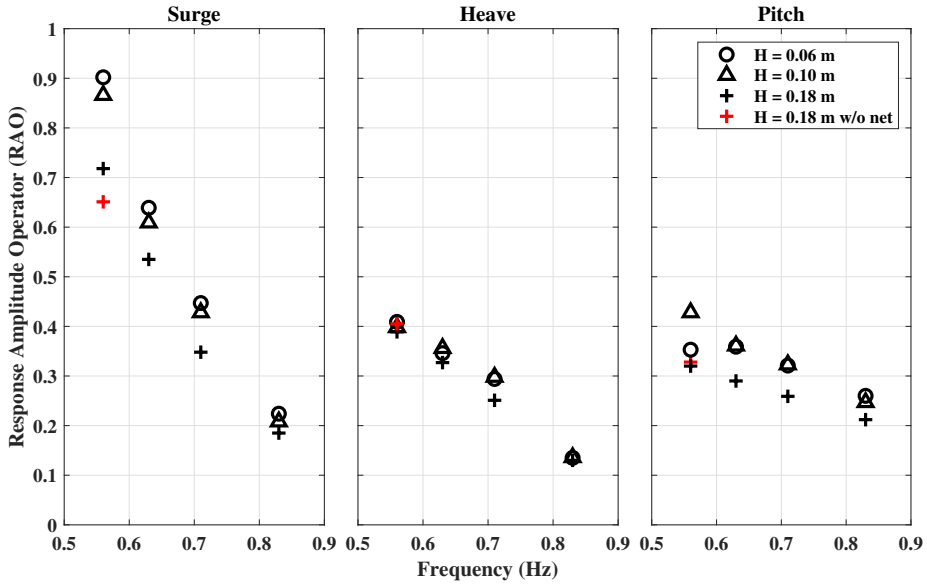

Figure 9: Translational and rotational motions of the "ShenLan 1" fish farm for varying wave heights (H) and wave frequencies.

4.1.2 Wave loads on the frame and maximum mooring tension forces

The non-linear external loads acting on the cylindrical frame structure consist of the mooring restoring forces and wave forces. The horizontal wave forces on the frame for different parameters in the head wave are presented in Fig. 12(a). In contrast to the RAOs, H and T show similar effects on the horizontal loadings due to the ultimate correlations with wave energies. It can be noted that the linear harmonic term increases with T and plays a dominant role in the predicted total force amplitudes. The Keulegan–Carpenter number KC for the thinnest cylindrical frames in the typical regular wave case (H = 0.18 m, T = 1.8 s) of this study is approximately 84, suggesting that viscous effects are playing an essential role in the total drift forces. The increased wave-overtopping and viscous effects around the considerable surge motion (T = 1.8 s) account for the gradual increase of the higher-order terms, which has also been verified in Kristiansen (2010); Martin et al. (2020). But, they are less sensitive to the wave parameters and are generally below 5% of the total horizontal drift loads. The importance of the mean component increases with increasing wave height due to increasing drift forces.

In contrast to the horizontal forces, the mean component of the vertical forces (Fig. 12(b)) is less influenced by the wave parameters and is the dominant factor in the total loads. A possible explanation for the independence from the wave input is the lack of the dominated viscous drag components in the vertical wave forces. The linear components show an increasing trend with H as the vertical velocities of the wave particles increase with H based on Stokes wave theory. The higher-order harmonics terms are again small (1%∼5% of the overall vertical load).

The expected mooring tension forces in wave fields are an essential part of the design process because it is directly related to the constraints and safety of the aquaculture farm.

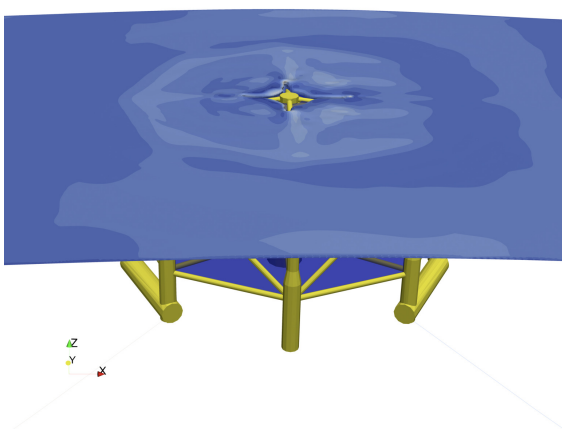

(a) H = 0.06 m, T = 1.8 s

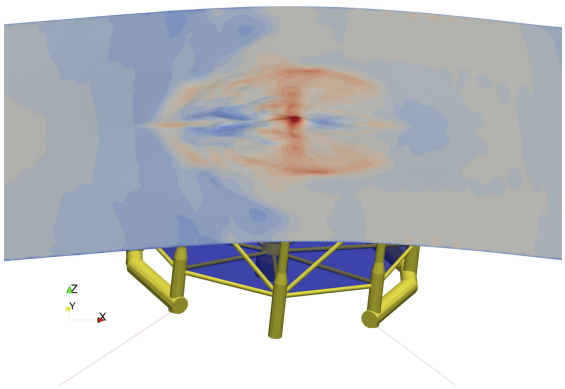

(b) H = 0.18 m, T = 1.8 s

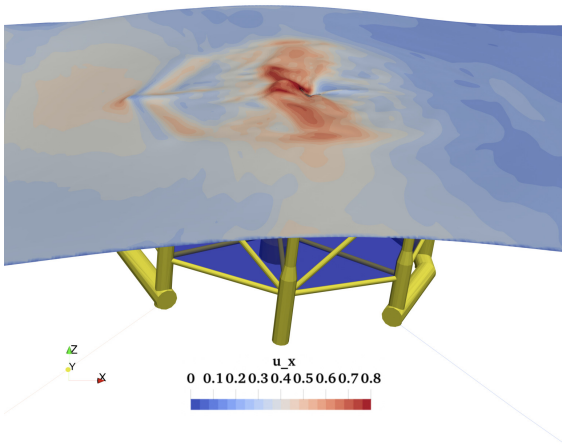

(c) H = 0.18 m, T = 1.2 s

Figure 10: Free surface contours showing the horizontal velocities in a wave crest situation of the "ShenLan 1" farm for different wave heights and periods.

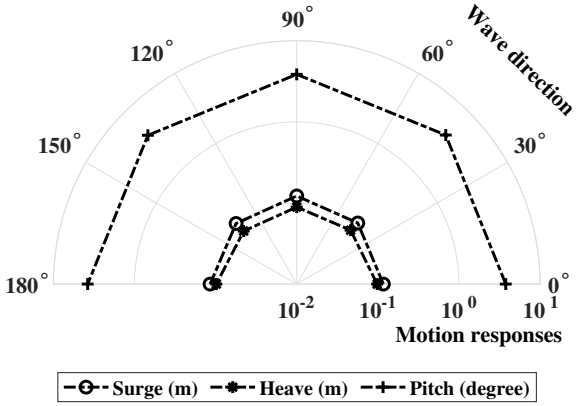

Figure 11: The motion responses of the fish farm model with the variations of wave-incoming directions (see more details in Tab. 5 for the definition of the motion responses).

In this study, the maximum tension forces at the windward and leeward mooring lines are extracted because of the geometrical symmetry of the four-point mooring system. The results are shown in Fig. 13. It is evident that the tension forces on the windward side are larger than on the leeward side due to the wave crest damping and momentum loss of the fluid while passing the structure. Moreover, it can be observed that the forces are proportional to T because of the enhanced motion responses. One can further notice that the increasing trend with H for the smallest T is less significant than for the larger T. This is in agreement with the experimental measurements in Zhao et al. (2019). In general, the forces are related to the motion responses so that maximum forces are predicted at the largest H and T. The following studies of the influence of the net solidity and ARs are performed for the wave input of H = 0.18 m and T = 1.8 s.

The horizontal and vertical wave forces on frames, as well as the horizontal wave force on nets, are shown in Fig. 14 with wave incident angles. There is no distinct difference between head wave and beam wave cases, while the hydrodynamic properties of cases with 45° and 135° wave incident directions are illustrated differently with head and beam wave cases. It is attributed to the various parts of the fish farm model encountering the incident waves, such as angles formed by mooring lines and the incident waves. In detail, the impacts are visible in terms of the second-order force components horizontally and vertically, which take a minor role in the total forces. The second-order horizontal terms in the cases of 45° and 135° directions are slightly lower than the head and beam wave cases, while it is presented as the distinct results for the vertical forces. The second-order wave forces on nets have a larger significance in the cases of 45° and 135° directions than in the head and beam wave cases. As for the maximum mooring line tensions, both windward and leeward amplitudes in 45° and 135° cases are more significant than that in the head and beam wave scenarios since they remain parallel with the wave incident directions. The sideward mooring tensions also appear with the minimum amplitudes in 45° and 135° cases. However, this further indicates that the influences of wave incidence angles on the breaking tensions of mooring chains should be fully considered during operations.

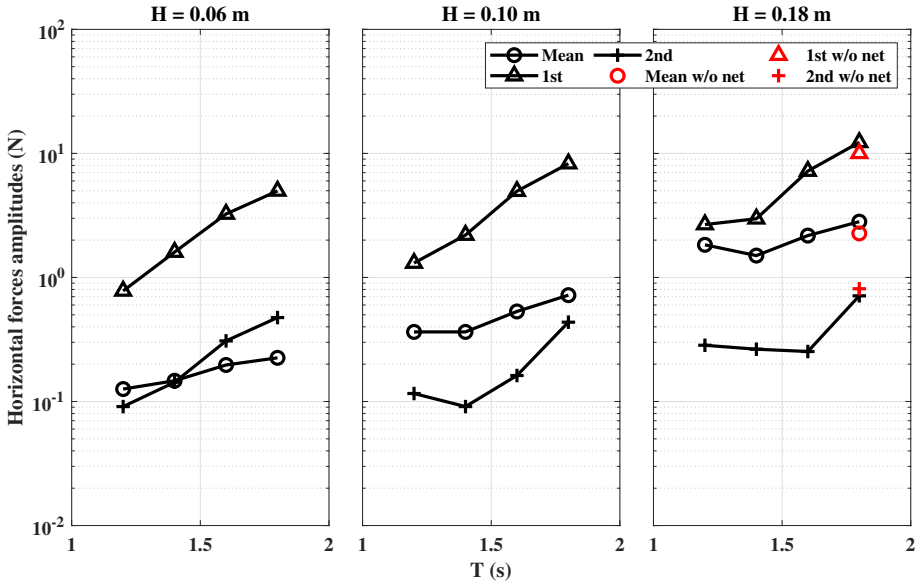

(a) Horizontal forces on the frame structure

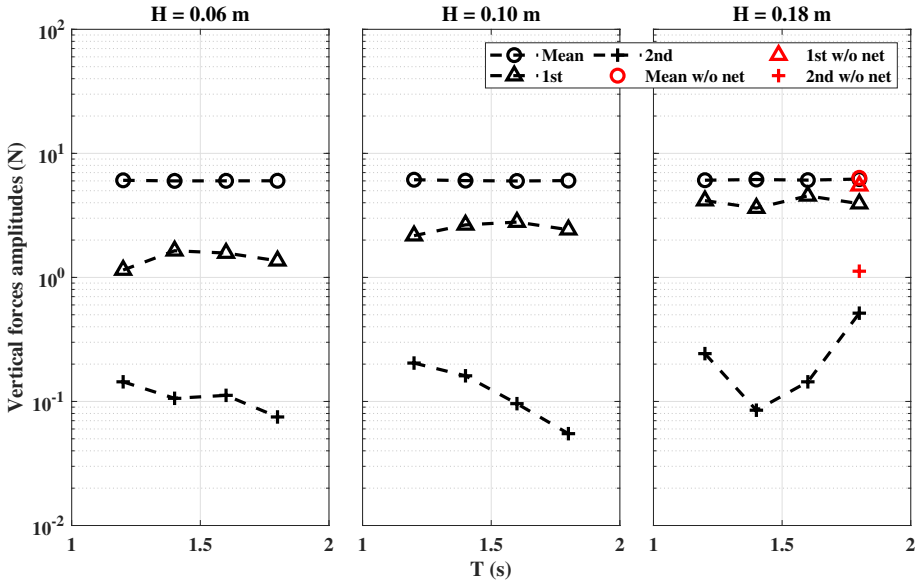

(b) Vertical forces on the frame structure

Figure 12: Load amplitudes on the "ShenLan 1" frame structure.

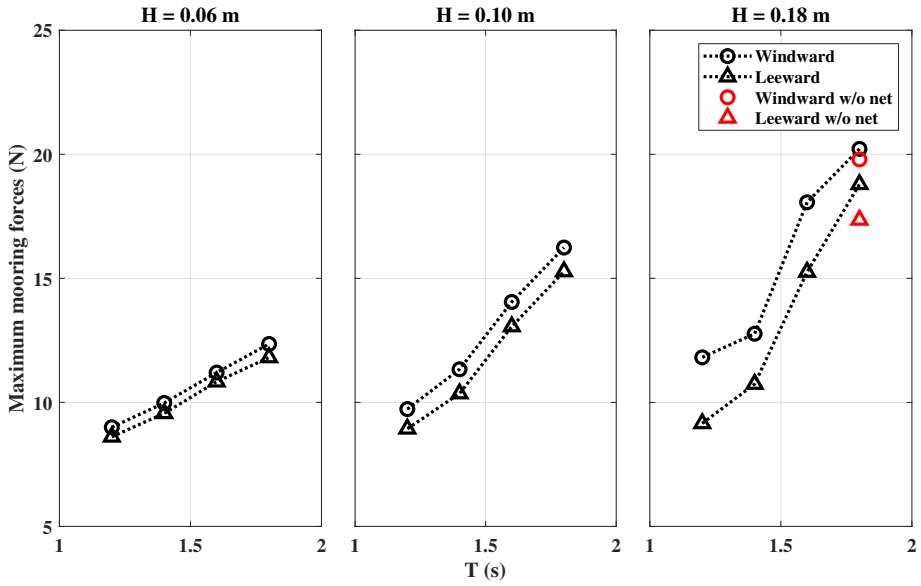

Figure 13: Maximum tension forces in the mooring chains for varying wave parameters.

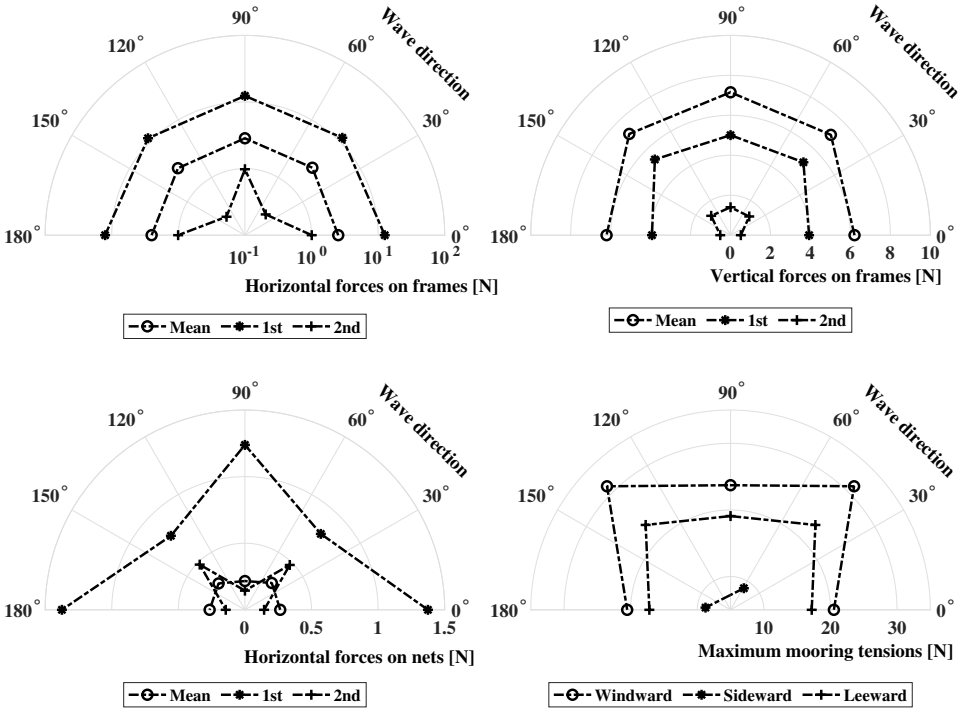

Figure 14: The horizontal and vertical wave forces on frames as well as the horizontal wave force on nets with the variations of wave-incoming directions.

4.2 Effects of the net sheets on the hydrodynamics of the fish farm

A comparative analysis of the motion responses and wave loadings related to simulations with and without net systems is discussed in the following section. For this purpose, results without nets are added to Fig. 9, 12 and 13 for H = 0.18 m and T = 1.8 s. It can be seen that the net is less important for the motion responses and maximum mooring tension forces than the wave parameters. The pitch motion presents the least difference as it is linked to the mooring system Sirigu et al. (2020), followed by a 4% relative difference for the heave motion and 10% decrease of the surge motion. The variation of the surge motion is related to the changed front area interacting with the fluid, as also noted in the experiments of "Ocean Farm 1" Zhao et al. (2019); Jin et al. (2021).

Next, the comparison of the horizontal and vertical loads on the "ShenLan 1" model with and without nets is presented in Fig. 12. It is shown that there is no significant difference in the horizontal forces on the frames. However, the additional effects of the nets on the second-order component of the vertical wave loads are visible. According to the second-order Stokes wave theory, the transient horizontal wave-particle velocities are significantly larger than the vertical components in most instances during transmissions, so the horizontal momentum losses behind net sheets are minor (compare in Fig. 20). However, the reduction of the vertical velocity components for lower magnitudes seems explained by the top and bottom cone nets equipped with the frames of "ShenLan 1" fish farm. Besides, the top nets in the working-state fish farm encounter frequent partial submersion and wave-overtopping over half a period (see Fig. 15). This explains the variation of the high-order components of the vertical accelerations between the farm with and without the net system.

Further, the relation between the horizontal loads on the net and the wave parameters is shown in Fig. 16. It can be noticed that the mean, linear and second-order horizontal loads on the rigid net tend to increase with steeper waves. For a deeper insight, Fig. 16(b) shows the percentage of the total forces related to the forces on the net for different waves. It can be seen that the proportions of the mean, linear and second-order components decrease from 55% to 10% with increasing T, but that there is no distinct trend visible for varying H. The larger proportion of the loads on net systems in high-frequency wave exactions might be attributed to the fact that the horizontal wave loads on the frame parts increase rapidly with T while that on the net sheets remain nearly constant in steep and shallow waves. Additionally, this is opposed to the clarification in Liu et al. (2021) that the drag forces on nets are relatively small compared to that on frames of the "Ocean Farm 1" model in pure current conditions. Thus, the consideration of waves in this study is more practical for offshore environments by including the non-linear wave-structure interaction effects.

Finally, the relevance of varying net solidities S_n for the hydrodynamics of the studied fish farm is shown in Fig. 17. The variation of the net solidity is achieved through changing the twine diameter while keeping the twine lengths constant. This corresponds to regular practices for preventing fish from escaping and bio-fouling issues. It is noticeable that the motion responses, the horizontal loads as well as the maximum mooring tension forces are less influenced by the variation of the net solidity which is in agreement with Miao et al. (2021). The horizontal forces on the nets gradually increase with the increase of S_n, which can be attributed to the positive correlations between drag forces and net solidities Wang et al. (2021), as well as more significant non-linear effects. In comparison with the horizontal wave forces on frames, the second-order term of forces on nets plays the same dominating role as

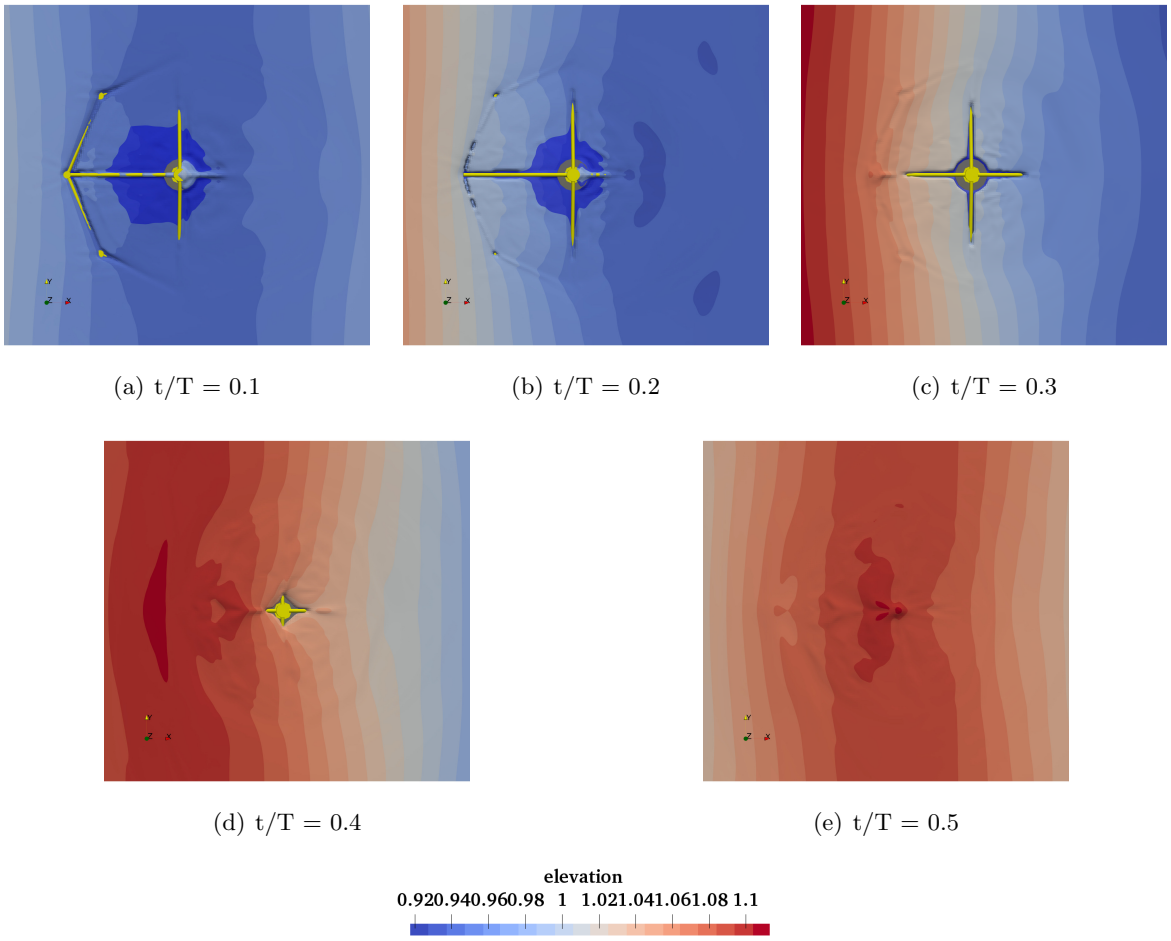

(a) t/T = 0.1 (b) t/T = 0.2 (c) t/T = 0.3

(d) t/T = 0.4 (e) t/T = 0.5

Figure 15: Wave propagating over the top of the "ShenLan 1" model at 0.53 m draught (production condition) over half a period.

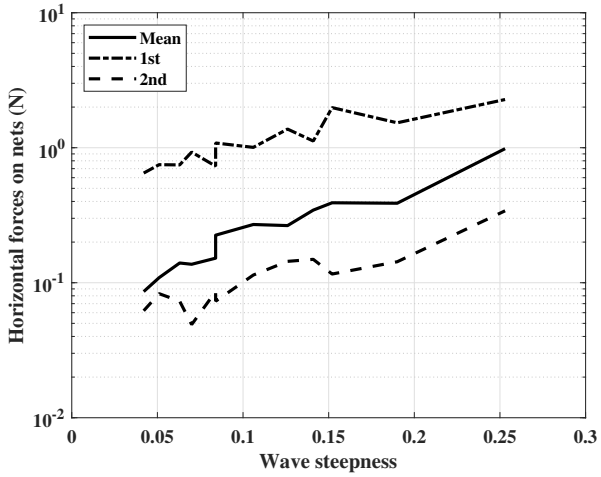

(a) Horizontal forces on the net sheets.

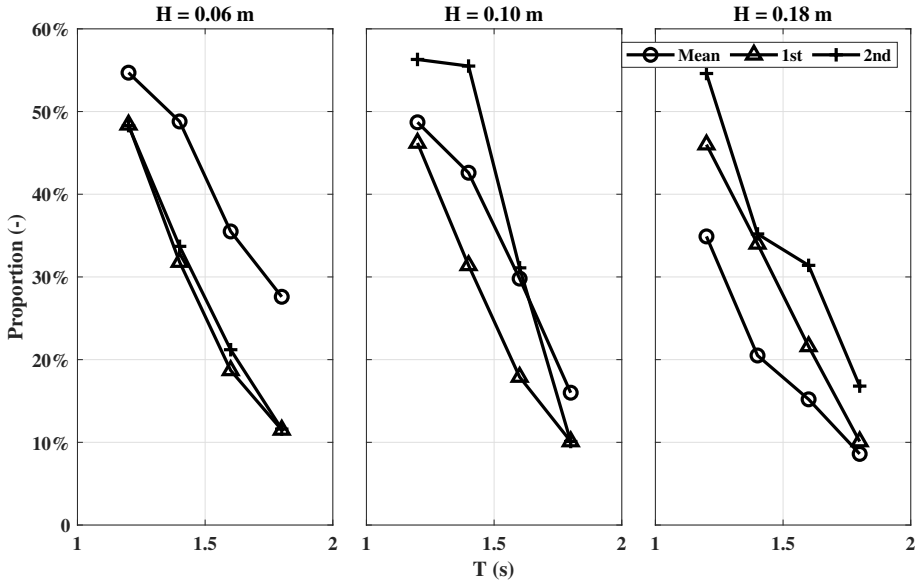

(b) The percentage of horizontal forces related to the total forces on the nets.

Figure 16: Amplitudes and percentages of drag forces related to the net system for varying wave parameters.

the mean part, indicating the distinct differences between nets and frames. Furthermore, the percentage of the horizontal forces related to the components on nets increases from below 5% to 32%, especially for the second-order harmonic term. This indicates that the non-linearity of the interaction plays an increasing importance in the overall assessment of the hydrodynamics with increasing S_n.

4.3 Effects of the draught on the hydrodynamics of the fish farm

The draught of the farm is varied by filling ballast tanks placed on the bottom of the structure. Thereby, the COG as well as the moments of inertia change accordingly Liu and He (2019). Two additional draughts are considered in this study: a draught of 0.19 m which corresponds to the overhauling condition and 0.38 m which represents the net-drying situation. To meet the actual environmental scenarios, the adjustments of draughts are conducted with the lowest H and T for the sake of safety. Therefore, a shorter investigated wave with the less H (H = 0.06 m, T = 1.2 s) is chosen to examine the hydrodynamics while changing draughts, representing the calm sea-state. As can be seen in Fig. 18, the translational motions show a gradual decrease with increasing draught for the investigated wave. The surge, heave and pitch motions decrease by 30.0%, 59.1% and 61.9% separately while transitioning from 0.19 m to 0.53 m. The variation of the maximum mooring tension forces follows the draught as well. Here, the weight of the catenary increase with decreasing draught, resulting in the larger vertical restoring forces.

In comparison, the surge, heave and pitch motions decrease by only 15.9%, 19.0% and 46.2% for the "Ocean Farm 1" model with increasing draught from 7 cm to 36 cm, respectively Liu et al. (2020). The differences between these two models are attributed to the larger AR of the "Ocean Farm 1" model and different wave inputs in this study. Furthermore, the draught has a more dramatic influence on the heave and pitch motions than the surge motion. As mentioned before, the heave and pitch motion could be dominated by the restoring effect from the mooring system which acts rather vertically than horizontally. A possible explanation is that both windward and leeward mooring tensions decline significantly with the draughts rise, so the degrees of the restoring effects from mooring lines are shrinking with the larger draughts. Moreover, both windward and leeward mooring restoring forces increase by 36%-38% between the operation and overhauling state. Therefore, the duration of the maintenance should be declined to avoid accumulated fatigue of the mooring chains.

The horizontal loads on the frame structure and nets are illustrated in Fig. 19. The most considerable wave loads on frames occur at a draught of 0.19 m. The occurrence of this circumstance is related to the placement of the structure in this condition. The largest areas of attack, which are the pontoons and water & air tanks at the bottom of the structure, are located close to the free surface where the highest wave action is expected. But this cannot apply to the wave loads on nets, which takes a little immersed volume compared with steel-frame. The considerable wave loads on nets, especially for the linear term, can be observed with the 0.53 m draught, hinting the close correlations with top cone nets under the close-to-submerged production conditions. It can be justified in Fig. 15 and Wang et al. (2021). Further, the mean horizontal components on the frames increase with increasing draught because of the increasing viscous portion from a larger immersed volume in the tank. However, the linear and second-order terms decrease from 0.19 m to 0.38 m and change negligibly from 0.38 m to 0.53 m. This can be understood through the visualisation of the

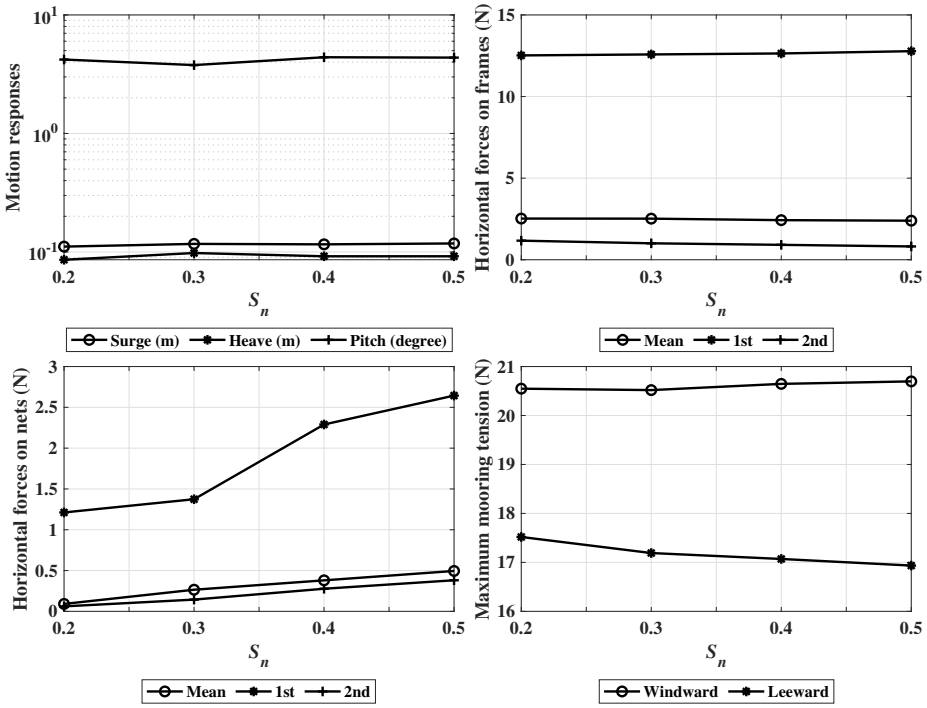

(a)

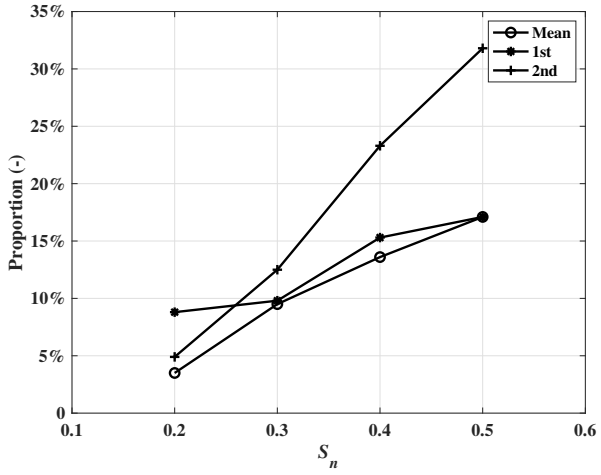

(b)

Figure 17: Hydrodynamics of the model with varying net solidities (a) (see more details in Tab. 5 for the definition of the motion responses). The percentage of horizontal forces related to net forces for varying net solidities (b).

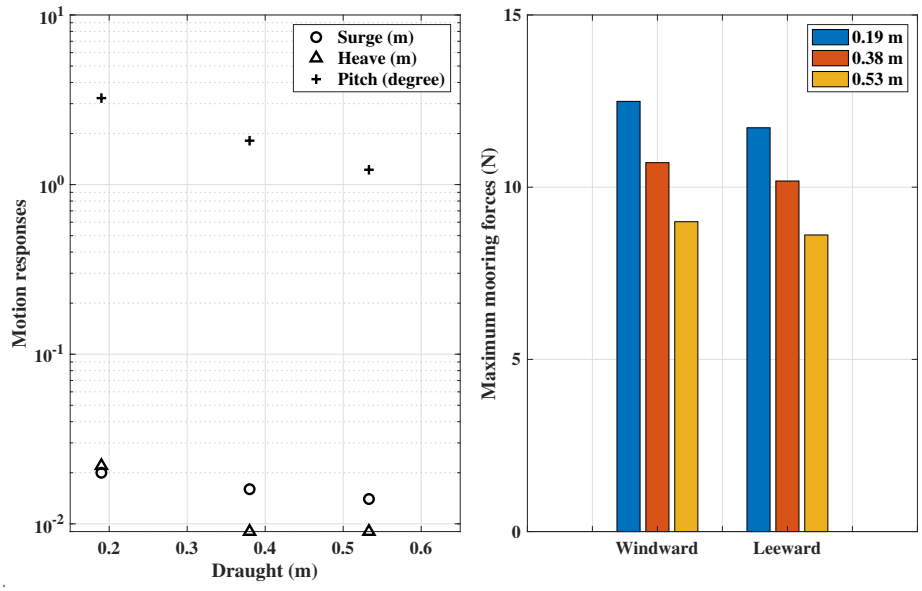

Figure 18: motion responses and maximum mooring tension forces of the fish cage for different draughts. See Tab. 5 for the definition of the motion responses.

free surface passing the farm at 0.38 m in Fig. 20. Frequent wave-overtopping and submersion of the disk-shaped oxygenation device attached to the central column occur at this draught. Consequently, the dramatic wave-structure interaction and fluctuations of the drift forces are expected.

4.4 Effect of the aspect ratio on the hydrodynamics of the fish farm

The effect of the structural AR on the hydrodynamics of the farm is illustrated in Fig. 21. Here, the overall diameter CL is modified while CH is kept unchanged to vary AR between 1.0 and 2.5. The fairleads and anchor points of the mooring lines are moved accordingly so that the total lengths of the catenary chains remain constant. The practical water depth limits the change of CH in the operation site. The COG position, weights, moments of inertia are varied consistently with the change of AR. The surge motion presents the decline by 24.07% with the rise of AR to 2.5, whereas the heave and pitch motions decrease by 59.36% and 82.74% in the process, respectively. At the same time, the pitch frequency decreases significantly (see Tab. 6). It is shown in Fig. 21 that both the maximum mooring tension forces in the front and aft lines are reduced significantly, following the correlation amongst mooring tension forces, heave and pitch motions described in Section 4.1.1. The amplitudes of motion responses decrease with the rise of AR, leading to the reductions of added mass effects of the structure in waves Faltinsen (1993). This has accounted for the decline of the linear and second-order wave forces with AR. The increased areas of exposed net sheets, especially at the bottom cone regions, can be the reason for the direct correlation with the drag forces on the nets and the mean horizontal forces on AR, respectively. But, this correlation is not noticeable for the frame structure. In summary, the increase of AR through enlarging the overall diameters results in smaller amplitudes of the motions and mooring forces.

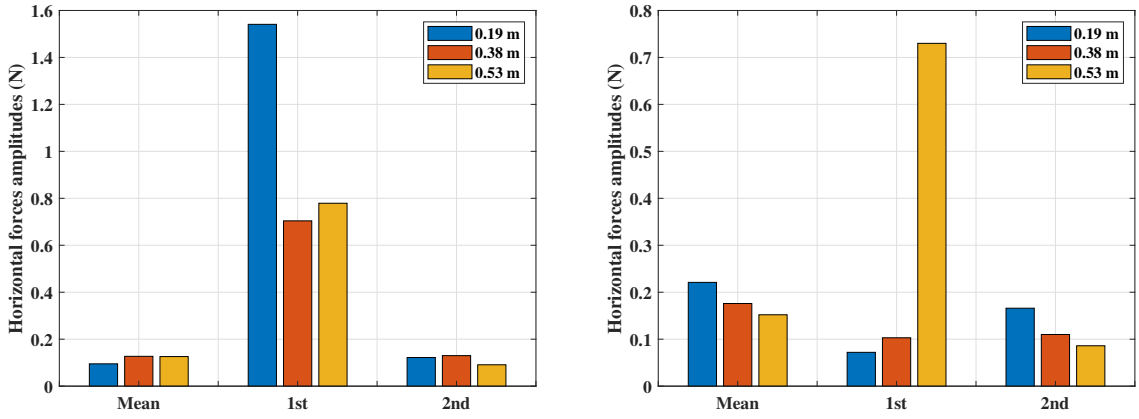

(a) Horizontal loadings on frames

(b) Horizontal loadings on nets

Figure 19: Amplitudes of the horizontal forces on the frame and the net system for varying draughts.

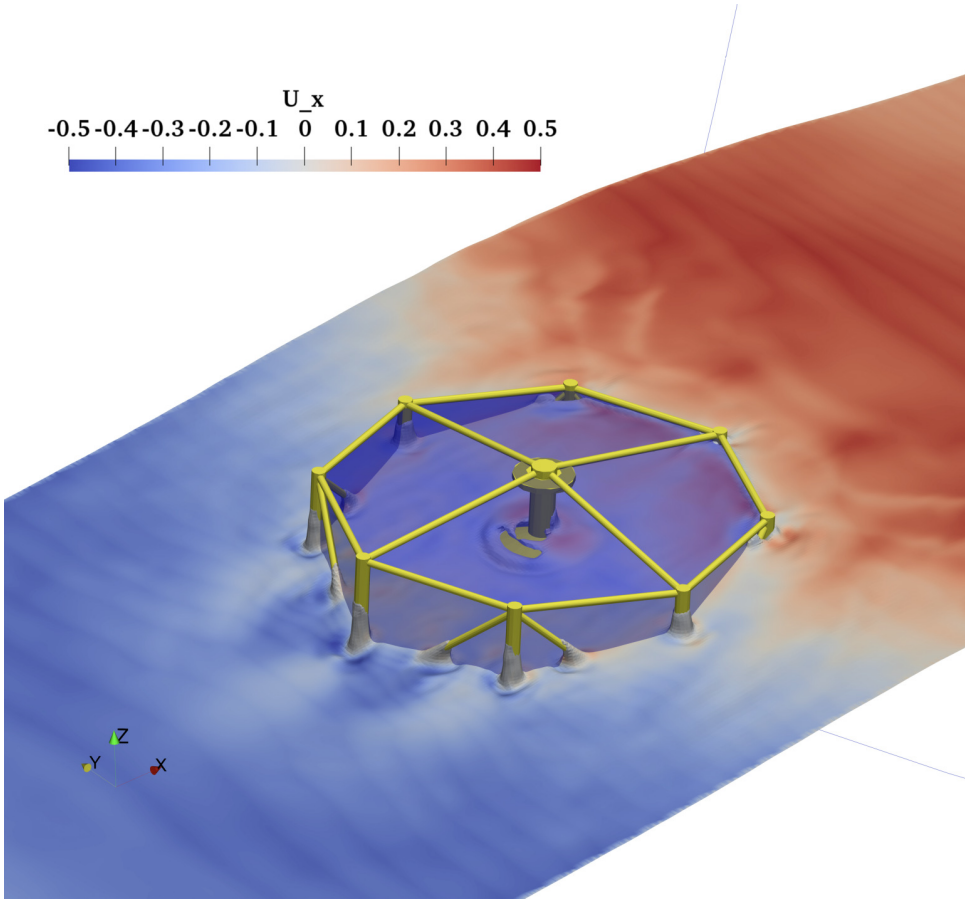

Figure 20: Free surface passing the fish farm at 0.38 m draught.

Table 6: The result of natural frequencies of heave and pitch motions with ARs

AR	**1.0**	**1.5**	**2.0**	**2.5**
ω_n (Heave)	3.11	3.35	2.46	3.18
ω_n (Pitch)	2.25	0.72	0.49	0.40

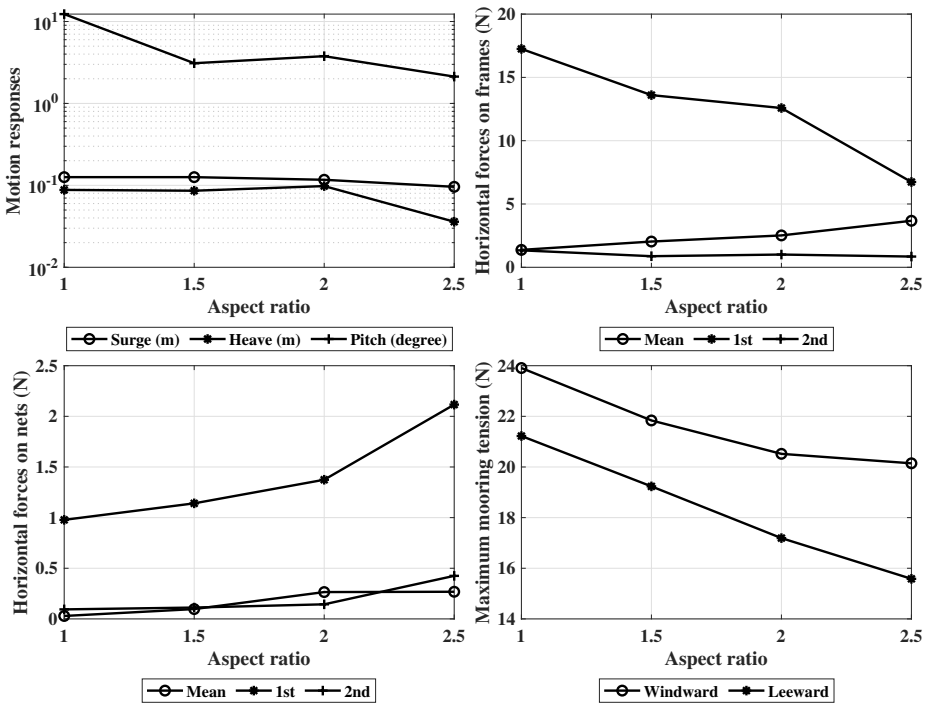

Figure 21: Hydrodynamics of the model with varying AR. See Tab. 5 for the definition of motion responses.

5 Conclusions

In this study, the hydrodynamic properties, including the motion responses and forces on the circular "ShenLan 1" fish farm are numerically modelled in waves. The free surface in the numerical wave tank is captured using the level set method. The moored-floating rigid body motion is directly coupled to the viscous fluid solution using a continuous direct method. Further, a static catenary solution is utilised for simulating the mooring system. The hydrodynamic loads on the rigid net panels are predicted using the simulation-based screen force model. The coupling of the net and fluid dynamics solver is achieved with a momentum loss term in the fluid dynamic equations.

First, the accuracy of the chosen numerical framework was validated for a vertical cylindrical floater and a circular fish farm model in waves. In contrast to the classical screen force model, the simulation-based screen force model shows improved results for the velocity reductions and hydrodynamic loads of a net panel in waves and currents. Finally, the effects

of varying wave parameters, net configurations, draughts, and structural variations on the hydrodynamic of the studied fish farm were discussed in detail. The main conclusions from this study are:

- The motion responses of the farm decrease with increasing wave frequency. The surge motion is more sensitive to the wave heights and periods compared to the heave and pitch motions because of the restrain from the mooring system. The wave incident angles cannot affect the motion responses.

- The increase of the wave height and length leads to increased horizontal loads on the frames, especially for the linear component. In contrast, the vertical components are quantitatively less impacted by varying wave parameters due to the lack of the dominated viscous drag component in the vertical direction. No distinct difference in wave loads and mooring tensions can be seen between head and beam wave cases, while the cases with 45° and 135° wave incident directions present differently with head and beam wave cases.

- The nets have only minor influences on the motion responses of the structure compared to the waves and mooring restoring effects. The hydrodynamic loads on the nets tend to increase with steeper waves. The percentage of horizontal forces attributed to nets decreases from 55% to 10% with increasing wave period. Additionally, the increase in the net solidity contributes to a 30% rise in the total drag forces.

- The motion responses are sensitive to the variations of draughts in the calm sea-state. The maximum mooring tension forces increase by 36%-38% from the operation to overhauling states. The most considerable loads on the frames occur at a draught of 0.19 m, while that on nets appear at the production state.

- The increase of the aspect ratio through enlarging the overall diameters results in a reduction of the motion amplitudes and mooring forces.

The coupled numerical model can be applied for further investigations of the structure in current and wave-current scenarios. The flow distributions around the fish farm in currents imply greater importance for the distribution and transportation of dissolved oxygen. The rotational motions of the structure become less important in currents, whereas the transitional offset is critical Jin et al. (2021) for the windward mooring lines. In this context, the investigation of mooring line failures is a relevant case to study as well. The Froude scaling effects on the offshore fish farm deserves a systematic discussion in the further investigations, as the differences of flow fields properties, such as vortex and bubble separations, can be introduced through the scaling Schmitt and Elsäßer (2017).

A Definition of the coefficients used in the simulation-based screen force model

The polynomial expressions for the drag and lift force coefficients at $\theta = 90°$ and 45°, derived from the Kriging metamodeling, are

$$
\begin{aligned}
C_{d,\theta=90^\circ;l,\theta=45^\circ} &= a_1 u_{rel} + a_2 d + a_3 l + a_4 u_{rel} d + a_5 u_{rel} l + a_6 dl + a_7 u_{rel}^2 + a_8 d^2 + a_9 l^2 + a_{10}, \\
C_{d,\theta=45^\circ} &= a_1 u_{rel} + a_2 d + a_3 l + a_4 u_{rel} d + a_5 u_{rel} l + a_6 dl + a_7 u_{rel}^2 + a_8 d^2 + a_9 l^2 + a_{10} u_{rel}^3 + \\
&\quad a_{11} l^3 + a_{12} u_{rel} dl + a_{13} u_{rel} d^2 + a_{14} u_{rel} l^2 + a_{15} d u_{rel}^2 + a_{16} dl^2 + a_{17} l u_{rel}^2 + a_{18} l d^2 + \\
&\quad a_{19} l d^3 + a_{20}, \qquad (19) \\
&\quad (0.1\ m/s < u_{rel} < 1\ m/s, 0.5\ mm < d < 3\ mm, 0.01\ m < l < 0.03\ m)
\end{aligned}
$$

with the constants $a_i,\ i = 1, ..., 20$, given in Tab. 7.

Table 7: The constants used in the polynomial fitting in Eq. (19).

	$C_{d,\theta=90^\circ}$	$C_{d,\theta=45^\circ}$	$C_{l,\theta=45^\circ}$
a_1	-0.132	-0.123	-0.063
a_2	340.797	205.486	66.287
a_3	-59.643	-40.789	-10.84
a_4	-9.129	-22.592	-11.374
a_5	2.245	-10.21	1.386
a_6	-12473.957	-12828.831	-2605.979
a_7	0.063	0.297	0.036
a_8	27831.591	60436.89	9838.141
a_9	1458.245	1787.102	267.245
a_{10}	0.619	-0.121	0.113
a_{11}	-	-24020.784	-
a_{12}	-	706.455	-
a_{13}	-	3775.06	-
a_{14}	-	253.464	-
a_{15}	-	-9.623	-
a_{16}	-	128457.65	-
a_{17}	-	-0.025	-
a_{18}	-	-21641.925	-
a_{19}	-	-9227634.55	-
a_{20}	-	0.368	-

Acknowledgment

The authors are grateful for the grants provided by the National Key Research and Development Program of China (Project No. 2019YFD0901000), Research Council of Norway HAVBRUK2 project (No. 267981) and the State Foundation for Visiting Ph.D. student from China Scholarship Council (No. 201906330049). The computations were performed on resources provided by UNINETT Sigma2 - the National Infrastructure for High Performance Computing and Data Storage in Norway (`http://www.sigma2.no`) under project No. NN2620K, and the Center for High Performance Computing and System Simulation, Pilot National Laboratory for Marine Science and Technology (Qingdao).

CRediT authorship contribution statement

Gang Wang: Conceptualisation, Validation, Investigation, Writing the original manuscript, Review. **Tobias Martin:** Conceptualisation, Methodology, Writing, Review. **Liuyi Huang:**

Data acquisition, Project administrations, Funding acquisition, Resources, Review, Supervision. **Hans Bihs:** Conceptualisation, Supervision, Resources, Review.

Declaration of competing interest

The authors declare that they have no known competing financial interests or personal relationships that could have appeared to influence the work reported in this paper.

References

K. Grigorakis, G. Rigos, Aquaculture effects on environmental and public welfare – The case of Mediterranean mariculture, Chemosphere 85 (2011) 899–919. doi:10.1016/j.oceaneng.2022.11152810.1016/j.chemosphere.2011.07.015.

Y. I. Chu, C. M. Wang, J. C. Park, P. F. Lader, Review of cage and containment tank designs for offshore fish farming, Aquaculture 519 (2020) 734928. doi:10.1016/j.oceaneng.2022.11152810.1016/j.aquaculture.2020.734928.

A. Berge, "ocean farm 1" licence conversion, a bargain now at euro142 million, 2020. URL: https://salmonbusiness.com/ocean-farm-1-licence-conversion-a-bargain-now-at-e142-million/.

O. A. Drønen, Mariculture as fikk tilsagn om utviklingstillatelser (in norwegian), 2019. URL: https://www.kyst.no/article/mariculture-as-fikk-tilsagn-om-utviklingstillatelser/.

R. Mutter, De maas's huge chinese offshore fish farm nearly ready for stocking, 2020. URL: https://www.intrafish.com/aquaculture/de-maass-huge-chinese-offshore-fish-farm-nearly-ready-for-stocking/2-1-831047.

L. Li, Z. Jiang, A. V. Høiland, M. C. Ong, Numerical analysis of a vessel-shaped offshore fish farm, J. Offshore Mech. Arct. Eng. 140 (2018) 041201. doi:10.1016/j.oceaneng.2022.11152810.1115/1.4039131.

L. Li, Z. Jiang, M. C. Ong, W. Hu, Design optimization of mooring system: An application to a vessel-shaped offshore fish farm, Eng. Struct. 197 (2019) 109363. doi:10.1016/j.oceaneng.2022.11152810.1016/j.engstruct.2019.109363.

G. Løland, Current forces on and flow through fish farms, Ph.D. thesis, Norwegian University of Science and Technology, Trondheim, Norway, 1991.

Y. Zhao, C. Guan, C. Bi, H. Liu, Y. Cui, Experimental investigations on hydrodynamic responses of a semi-submersible offshore fish farm in waves, J. Mar. Sci. Eng. 7 (2019) 7070238. doi:10.1016/j.oceaneng.2022.11152810.3390/jmse7070238.

H.-F. Liu, C.-W. Bi, Y.-P. Zhao, Experimental and numerical study of the hydrodynamic characteristics of a semisubmersible aquaculture facility in waves, Ocean Eng. 214 (2020) 107714. doi:10.1016/j.oceaneng.2022.11152810.1016/j.oceaneng.2020.107714.

671 Y.-P. Zhao, H.-F. Liu, C.-W. Bi, Y. Cui, C.-T. Guan, Numerical study on the flow field inside
672 and around a semi-submersible aquaculture platform, Appl. Ocean Res. 115 (2021) 102824.
673 doi:10.1016/j.oceaneng.2022.11152810.1016/j.apor.2021.102824.

674 H.-F. Liu, C.-W. Bi, Z. Xu, Y.-P. Zhao, Hydrodynamic assessment of a semi-submersible
675 aquaculture platform in uniform fluid environment, Ocean Eng. 237 (2021) 109656.
676 doi:10.1016/j.oceaneng.2022.11152810.1016/j.oceaneng.2021.109656.

677 Y.-j. Miao, J. Ding, C. Tian, X.-j. Chen, Y.-l. Fan, Experimental and numerical study
678 of a semi-submersible offshore fish farm under waves, Ocean Eng. 225 (2021) 108794.
679 doi:10.1016/j.oceaneng.2022.11152810.1016/j.oceaneng.2021.108794.

680 T. Kristiansen, O. M. Faltinsen, Modelling of current loads on
681 aquaculture net cages, J Fluids Struct 34 (2012) 218–235.
682 doi:10.1016/j.oceaneng.2022.11152810.1016/j.jfluidstructs.2012.04.001.

683 X.-H. Huang, H.-Y. Liu, Y. Hu, T.-P. Yuan, Q.-Y. Tao, S.-M. Wang, Z.-X. Liu,
684 Hydrodynamic performance of a semi-submersible offshore fish farm with a single
685 point mooring system in pure waves and current, Aquac Eng 90 (2020) 102075.
686 doi:10.1016/j.oceaneng.2022.11152810.1016/j.aquaeng.2020.102075.

687 J. Jin, B. Su, R. Dou, C. Luan, L. Li, I. Nygaard, N. Fonseca, Z. Gao, Numer-
688 ical modelling of hydrodynamic responses of Ocean Farm 1 in waves and current
689 and validation against model test measurements, Mar. Struct. 78 (2021) 103017.
690 doi:10.1016/j.oceaneng.2022.11152810.1016/j.marstruc.2021.103017.

691 S. Yu, H. Qin, P. Li, Z. Xu, Nonlinear vertical accelerations and mooring loads of a semi-
692 submersible offshore fish farm under extreme conditions, Aquac Eng 95 (2021) 102193.
693 doi:10.1016/j.oceaneng.2022.11152810.1016/j.aquaeng.2021.102193.

694 G. Wang, T. Martin, L. Huang, H. Bihs, A numerical study of the hydrodynamics of an
695 offshore fish farm using REEF3D, J. Offshore Mech. Arct. Eng. in Press (2021) 1–10.
696 doi:10.1016/j.oceaneng.2022.11152810.1115/1.4052865.

697 T. Martin, A. Tsarau, H. Bihs, A numerical framework for modelling the dynamics of
698 open ocean aquaculture structures in viscous fluids, Appl. Ocean Res. (2020) 102410.
699 doi:10.1016/j.oceaneng.2022.11152810.1016/j.apor.2020.102410.

700 G. Wang, T. Martin, L. Huang, H. Bihs, An improved screen force model based on CFD
701 simulations of the hydrodynamic loads on knotless net panels, Appl. Ocean Res. 118 (2022)
702 102965. doi:10.1016/j.oceaneng.2022.11152810.1016/j.apor.2021.102965.

703 T. Martin, A. Kamath, G. Wang, H. Bihs, Modelling Open Ocean Aquaculture Structures
704 Using CFD and a Simulation-Based Screen Force Model, J. Mar. Sci. Eng. 10 (2022) 332.
705 doi:10.1016/j.oceaneng.2022.11152810.3390/jmse10030332.

706 A. C. Mayilvahanan, P. R. Selvam, Time Domain Response Analysis of Barge Floater
707 Supporting an Offshore Wind Turbine, Int. J. Ocean Clim. Syst. 2 (2011) 303–314.
708 doi:10.1016/j.oceaneng.2022.11152810.1260/1759-3131.2.4.303.

H. Bihs, A. Kamath, M. Alagan Chella, A. Aggarwal, Ø. A. Arntsen, A new level set numerical wave tank with improved density interpolation for complex wave hydrodynamics, Comput Fluids 140 (2016) 191–208. doi:10.1016/j.oceaneng.2022.11152810.1016/j.compfluid.2016.09.012.

S. Osher, J. A. Sethian, Fronts propagating with curvature-dependent speed: Algorithms based on Hamilton-Jacobi formulations, J. Comput. Phys. 79 (1988) 12–49. doi:10.1016/j.oceaneng.2022.11152810.1016/0021-9991(88)90002-2.

A. Aggarwal, H. Bihs, D. Myrhaug, M. A. Chella, Characteristics of breaking irregular wave forces on a monopile, Appl. Ocean Res. 90 (2019). doi:10.1016/j.oceaneng.2022.11152810.1016/j.apor.2019.06.003.

T. Cui, A. Kamath, W. Wang, L. Yuan, D. Han, H. Bihs, Focused Plunging Breaking Waves Impact on Pile Group in Finite Water Depth, J. Offshore Mech. Arct. Eng. 144 (2021) 031202. doi:10.1016/j.oceaneng.2022.11152810.1115/1.4053126.

G.-S. Jiang, C.-W. Shu, Efficient Implementation of Weighted ENO Schemes, J. Comput. Phys. 126 (1996) 202–228. doi:10.1016/j.oceaneng.2022.11152810.1006/jcph.1996.0130.

G.-S. Jiang, D. Peng, Weighted ENO Schemes for Hamilton–Jacobi Equations, SIAM J. Sci. Comput. 21 (2000) 2126–2143. doi:10.1016/j.oceaneng.2022.11152810.1137/S106482759732455X.

C.-W. Shu, S. Osher, Efficient implementation of essentially non-oscillatory shock-capturing schemes, J. Comput. Phys. 77 (1988) 439–471. doi:10.1016/j.oceaneng.2022.11152810.1016/0021-9991(88)90177-5.

L. J. P. Timmermans, P. D. Minev, F. N. Van De Vosse, An approximate projection scheme for incompressible flow using spectral elements, Int J Numer Methods Fluids 22 (1996) 673–688. doi:10.1016/j.oceaneng.2022.11152810.1002/(SICI)1097-0363(19960415)22:7¡673::AID-FLD373¿3.0.CO;2-O.

H. A. van der Vorst, Bi-cgstab: A fast and smoothly converging variant of bi-cg for the solution of nonsymmetric linear systems, SIAM J. Sci. Stat. Comput. 13 (1992) 631–644. doi:10.1016/j.oceaneng.2022.11152810.1137/0913035.

T. Martin, A. Kamath, H. Bihs, Accurate modeling of the interaction of constrained floating structures and complex free surfaces using a new quasistatic mooring model, International Journal for Numerical Methods in Fluids 93 (2) (2021) 504–526. doi:10.1016/j.oceaneng.2022.11152810.1002/fld.4894.

O. Faltinsen, Sea Loads on Ships and Offshore Structures, Cambridge Ocean Technology Series, 1st ed., Cambridge University Press, Cambriage, 1993.

T. Kristiansen, O. M. Faltinsen, Experimental and numerical study of an aquaculture net cage with floater in waves and current, J Fluids Struct 54 (2015) 1–26. doi:10.1016/j.oceaneng.2022.11152810.1016/j.jfluidstructs.2014.08.015.

Y. Yao, Y. Chen, H. Zhou, H. Yang, Numerical modeling of current loads on a net cage considering fluid-structure interaction, J Fluids Struct 62 (2016) 350–366. doi:10.1016/j.oceaneng.2022.11152810.1016/j.jfluidstructs.2016.01.004.

Y. Shen, M. Greco, O. M. Faltinsen, I. Nygaard, Numerical and experimental investigations on mooring loads of a marine fish farm in waves and current, J Fluids Struct 79 (2018) 115–136. doi:10.1016/j.oceaneng.2022.11152810.1016/j.jfluidstructs.2018.02.004.

T. Martin, A. Kamath, H. Bihs, A Lagrangian approach for the coupled simulation of fixed net structures in a Eulerian fluid model, J Fluids Struct 94 (2020) 102962. doi:10.1016/j.oceaneng.2022.11152810.1016/j.jfluidstructs.2020.102962.

T. Martin, H. Bihs, A non-linear implicit approach for modelling the dynamics of porous tensile structures interacting with fluids, J Fluids Struct 100 (2021) 103168. doi:10.1016/j.oceaneng.2022.11152810.1016/j.jfluidstructs.2020.103168.

J. V. Aarsnes, H. Rudi, G. Loland, Current forces on cage, net deflection., in: Engineering for offshore fish farming, 1990, pp. 137–152.

A. Koop, A. Bereznitski, Model-Scale and Full-Scale CFD Calculations for Current Loads on Semi-Submersible, in: Proceedings of the ASME 2011 30th International Conference on Ocean, Offshore and Arctic Engineering. Volume 7: CFD and VIV; Offshore Geotechnics., Rotterdam, The Netherlands, 2011, pp. 147–157. doi:10.1016/j.oceaneng.2022.11152810.1115/OMAE2011-49204.

P. Schmitt, B. Elsäßer, The application of Froude scaling to model tests of Oscillating Wave Surge Converters, Ocean Eng. 141 (2017) 108–115. doi:10.1016/j.oceaneng.2022.11152810.1016/j.oceaneng.2017.06.003.

Y. Wei, A. Rafiee, A. Henry, F. Dias, Wave interaction with an oscillating wave surge converter, Part I: Viscous effects, Ocean Eng. 104 (2015) 185–203. doi:10.1016/j.oceaneng.2022.11152810.1016/j.oceaneng.2015.05.002.

J. Palm, C. Eskilsson, L. Bergdahl, R. E. Bensow, Assessment of Scale Effects, Viscous Forces and Induced Drag on a Point-Absorbing Wave Energy Converter by CFD Simulations, J. Mar. Sci. Eng. 6 (2018) 124. doi:10.1016/j.oceaneng.2022.11152810.3390/jmse6040124.

O. M. Faltinsen, Y. Shen, Wave and Current Effects on Floating Fish Farms, J. Mar. Sci. Appl. 17 (2018) 284–296. doi:10.1016/j.oceaneng.2022.11152810.1007/s11804-018-0033-5.

T. Martin, H. Bihs, A Numerical Solution for Modelling Mooring Dynamics, Including Bending and Shearing Effects, Using a Geometrically Exact Beam Model, J. Mar. Sci. Eng. 9 (2021) 486. doi:10.1016/j.oceaneng.2022.11152810.3390/jmse9050486.

N. G. Jacobsen, D. R. Fuhrman, J. Fredsøe, A wave generation toolbox for the open-source CFD library: OpenFoam®, Int. J. Numer. Methods Fluids 70 (2012) 1073–1088. doi:10.1016/j.oceaneng.2022.11152810.1002/fld.2726.

H. Bihs, A. Kamath, A combined level set/ghost cell immersed boundary representation for floating body simulations, Int. J. Numer. Methods Fluids 83 (2017) 905–916. doi:10.1016/j.oceaneng.2022.11152810.1002/fld.4333.

785 G. Yao, Z. Ma, B. Ding, J. Wang, Statistical analysis of annual ultimate values of waves in
786 the Yellow Sea and the Bohai Sea (in Chinese), Harbor Engineering (in Chinese) 04 (1992)
787 31–37.

788 G. Moura Paredes, J. Palm, C. Eskilsson, L. Bergdahl, F. Taveira-Pinto, Experimental in-
789 vestigation of mooring configurations for wave energy converters, Int. J. Mar. Energy 15
790 (2016) 56–67. doi:10.1016/j.oceaneng.2022.11152810.1016/j.ijome.2016.04.009.

791 J. Palm, C. Eskilsson, G. M. Paredes, L. Bergdahl, Coupled mooring analysis for floating
792 wave energy converters using CFD: Formulation and validation, Int. J. Mar. Energy 16
793 (2016) 83–99. doi:10.1016/j.oceaneng.2022.11152810.1016/j.ijome.2016.05.003.

794 M. Griebel, T. Dornseifer, T. Neunhoeffer, Numerical simulation in fluid dynamics: a practical
795 introduction, SIAM, 1998.

796 G. M. Paredes, J. Palm, C. Eskilsson, L. Bergdahl, F. Taveira-Pinto, Experimental investi-
797 gation of mooring configurations for wave energy converters, in: 11th European Wave and
798 Tidal Energy Conference. At: Nantes, France, 2015, pp. 8B5–2.

799 C. W. Bi, Y. P. Zhao, G. H. Dong, T. J. Xu, F. K. Gui, Experimental investigation of the
800 reduction in flow velocity downstream from a fishing net, Aquac Eng 57 (2013) 71–81.
801 doi:10.1016/j.oceaneng.2022.11152810.1016/j.aquaeng.2013.08.002.

802 H. M. Føre, P. C. Endresen, C. Norvik, P. Lader, Hydrodynamic Loads on Net Panels With
803 Different Solidities, J. Offshore Mech. Arct. Eng. 143 (2021). URL: 10.1115/1.4049723.
804 doi:10.1016/j.oceaneng.2022.11152810.1115/1.4049723.

805 I. Tsukrov, A. Drach, J. Decew, M. Robinson Swift, B. Celikkol, Characterization of ge-
806 ometry and normal drag coefficients of copper nets, Ocean Eng. 38 (2011) 1979–1988.
807 doi:10.1016/j.oceaneng.2022.11152810.1016/j.oceaneng.2011.09.019.

808 S. Dong, X. You, F. Hu, Effects of wave forces on knotless polyethylene and chain-
809 link wire netting panels for marine aquaculture cages, Ocean Eng. 207 (2020) 107368.
810 doi:10.1016/j.oceaneng.2022.11152810.1016/j.oceaneng.2020.107368.

811 D. G. Alciatore, Introduction to mechatronics and measurement systems, Tata McGraw-Hill
812 Education, 2007.

813 S. R. Singiresu, Mechanical vibrations, Addison Wesley Boston, MA, 1995.

814 A. Çelik, A. Altunkaynak, Determination of hydrodynamic parameters of a fixed OWC by
815 performing experimental and numerical free decay tests, Ocean Eng. 204 (2020) 106827.
816 doi:10.1016/j.oceaneng.2022.11152810.1016/j.oceaneng.2019.106827.

817 D. W. Fredriksson, M. Swift, J. D. Irish, I. Tsukrov, B. Celikkol, Fish cage and mooring
818 system dynamics using physical and numerical models with field measurements, Aquac
819 Eng 27 (2003) 117–146. doi:10.1016/j.oceaneng.2022.11152810.1016/S0144-8609(02)00043-
820 2.

821 J. Pinkster, Low frequency second order wave exciting forces on floating structures, Ph.D.
822 thesis, Faculty of Marine Technology, Delft University of Technology, 1980.

823 D. Kristiansen, Wave induced effects on floaters of aquaculture plants, Ph.D. thesis, Depart-
824 ment of Marine Technology, Norwegian University of Science and Technology (NTNU),
825 2010.

826 S. A. Sirigu, M. Bonfanti, E. Begovic, C. Bertorello, P. Dafnakis, G. Giorgi, G. Bracco, G. Mat-
827 tiazzo, Experimental Investigation of the Mooring System of a Wave Energy Converter in
828 Operating and Extreme Wave Conditions, Journal of Marine Science and Engineering 8
829 (2020).

830 G. Wang, T. Martin, L. Huang, H. Bihs, Modeling the flow around and the hydrody-
831 namic drag on net meshes using REEF3D, J. Offshore Mech. Arct. Eng. (2021) 1–21.
832 doi:10.1016/j.oceaneng.2022.11152810.1115/1.4051408.

833 J. Liu, Y. He, The basic design and instructions of the offshore fish farm in YSCWM, Technical
834 Report, Chinese Institute of Marine & Offshore Engineering HB. Co., Ltd., 2019.